5.0 DEORBIT/ENTRY

5.1 INTRODUCTION

The deorbit and entry section is divided into four distinct areas. The first section discusses the upper atmosphere weather including high altitude winds, and the Kennedy Space Center (KSC) Shuttle Landing Facility (SLF) weather for the STS-107 landing. The next section includes a detailed discussion of forensics data obtained from testing and analysis of the key items in the recovered debris. The third section is a narrative of the entry events from February 1, 2003, and the fourth section is a brief discussion of key elements of the aerodynamic reconstruction.

5.2 WEATHER

5.2.1 Upper Atmosphere Weather

As the Shuttle entered the atmosphere, it descended from about 400,000 feet when located over the central Pacific Ocean to roughly 200,000 feet over Texas. The Goddard Space Flight Center Data Assimilation Office (DAO) provided the GEOS-4 model analysis for the investigation in order to provide a best estimate of the density, temperature, and wind along the entry trajectory. The GEOS-4 model assimilates a wide variety of data sources to produce an integrated 3-dimensional analysis of the atmosphere from the Earth's surface to about 250,000 feet. The Global Reference Atmosphere Model (GRAM) was used to provide information about the atmosphere from Entry Interface to the top of the GEOS-4 analysis. In general, the entry environment was characterized by a lower than average density and higher than average winds prior to the vehicle breakup. Comparison of the GEOS-4 analysis to GRAM indicates that the estimated density and winds were within the expected climatology for the upper atmosphere. Figure 5-1 shows the wind profile that was developed by the DAO as part of the STS-107 investigation.

5.2.2 Landing Weather

On the morning of February 1, 2003, there was a concern for ground fog formation at KSC for the first STS-107 landing opportunity. This concern is not uncommon for a morning landing at KSC during the winter months. The landing time for the first KSC opportunity was 9:16 EST. The forecast called for the fog to burn off as the sun rose, producing mixing in the lower levels of the atmosphere. The Shuttle Training Aircraft (STA), which is used for weather reconnaissance, flew approaches to both the KSC-15 and KSC-33 runways to determine the best runway for landing. The STA is used to evaluate touchdown conditions, visibility, turbulence, crosswind, and overall pilot workload. At the time of deorbit decision, runway visibility was reported as 4 miles in light fog with winds 5 knots from the west. Visibility on final approach was slightly better for Runway 33. The final landing runway decision was not made at that time.

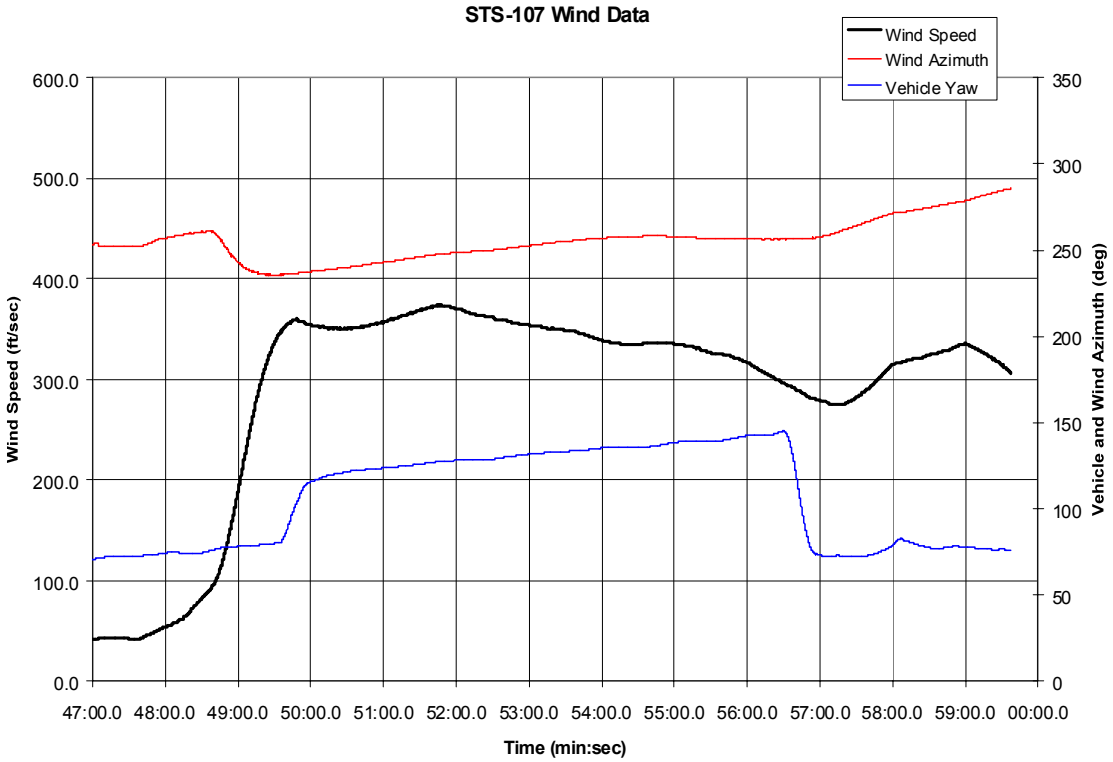

Figure 5-1. Wind profile developed by DAO as part of the STS-107 investigation (time referenced to 8:min:sec EST)

Leading up to the deorbit decision time, the fog had been the main point of discussion until some clouds developed to the northwest of the landing area. Satellite imagery indicated an area of broken clouds (5/8 to 7/8 sky coverage) with bases at approximately 4,000 feet above ground level between 20 and 25 nautical miles northwest of the runway. The forecast was for those clouds to erode as they approached the SLF producing scattered clouds (3/8 or 4/8 sky coverage) at landing time. The Spaceflight Meteorology Group (SMG) stated that if erosion did not occur, the clouds reaching the SLF would be covering the runway for the first landing opportunity. No low clouds were being reported at the SLF at deorbit burn decision time and no surrounding observing sites were reporting low ceilings. The final forecast update was for a few clouds at one thousand feet and scattered clouds at three thousand feet, and the forecast remained "Go" per the flight rules.

At the actual deorbit decision time and at the actual deorbit time, the landing weather satisfied all criteria per the documented Flight Rules, resulting in a "Go" observation and a "Go" forecast. At 9:10 EST, approximately five minutes prior to the expected landing time, the weather observation at the SLF reported a broken ceiling at 3,500 feet with 6/8 sky coverage and visibility 7 miles. The ceiling remained 3,500 broken until 9:25 EST at which time the SLF observer reported scattered clouds with 3/8 sky coverage.

The cloud deck at landing time was below the Flight Rule ceiling minimum requirement of 8,000 feet. Therefore, the commander would have relied in part on computer instrumentation and visible geographic references of the airfield, flying a Microwave Scanning Beam Landing System (MSBLS) approach until breaking out of the clouds at 3,500 feet, a procedure regularly practiced in several landing simulators. The incorporation of MSBLS data provides very accurate onboard navigation, allowing for more accurate instrument information and facilitating instrument approach capability. The opinion among several experienced astronaut commanders, including the Chief of the Astronaut Office, is that the landing would likely not have been affected by this ceiling, when considering all other conditions of the day.

5.3 HARDWARE FORENSICS

As discussed earlier in Section 3, Columbia entered the upper atmosphere with unknown damage to a Reinforced Carbon-Carbon (RCC) panel or Tee seal in the left wing RCC panels 6 through 9 area. The panel 8/9 area is the most likely area of damage as determined by hardware forensics testing, and analysis of MADS entry temperature and strain measurements on the left wing leading edge structure. This damage area is also consistent with the location of the ascent foam impact, and includes the Tee seals adjacent to panel 8, Tee seals 7 and 8.

The forensic data indicate that the panel 8/9 area was subjected to extreme entry heating over a long period of time leading to RCC rib erosion, severely slumped carrier panel tiles, and a substantial slag deposition on the upper portion of RCC panels 8 and 9. Figure 5-2 shows the slag deposition (both metallic and oxide) in the RCC panel 8/9 area relative to the other parts of the wing leading edge, and Figure 5-3 shows samples of the severe slag deposition on the panel 8 rib. A review of all recovered debris indicates that this is the most probable area of a breach into the wing since there are no other debris pieces that exhibit the unique characteristics observed in this area.

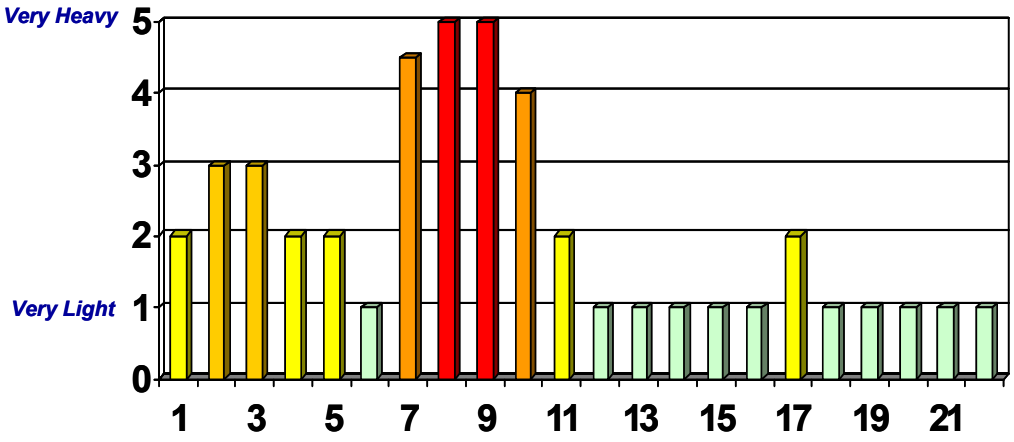

Figure 5-2. Slag deposition in the RCC panel 8/9 area relative to the other parts of the left wing leading edge

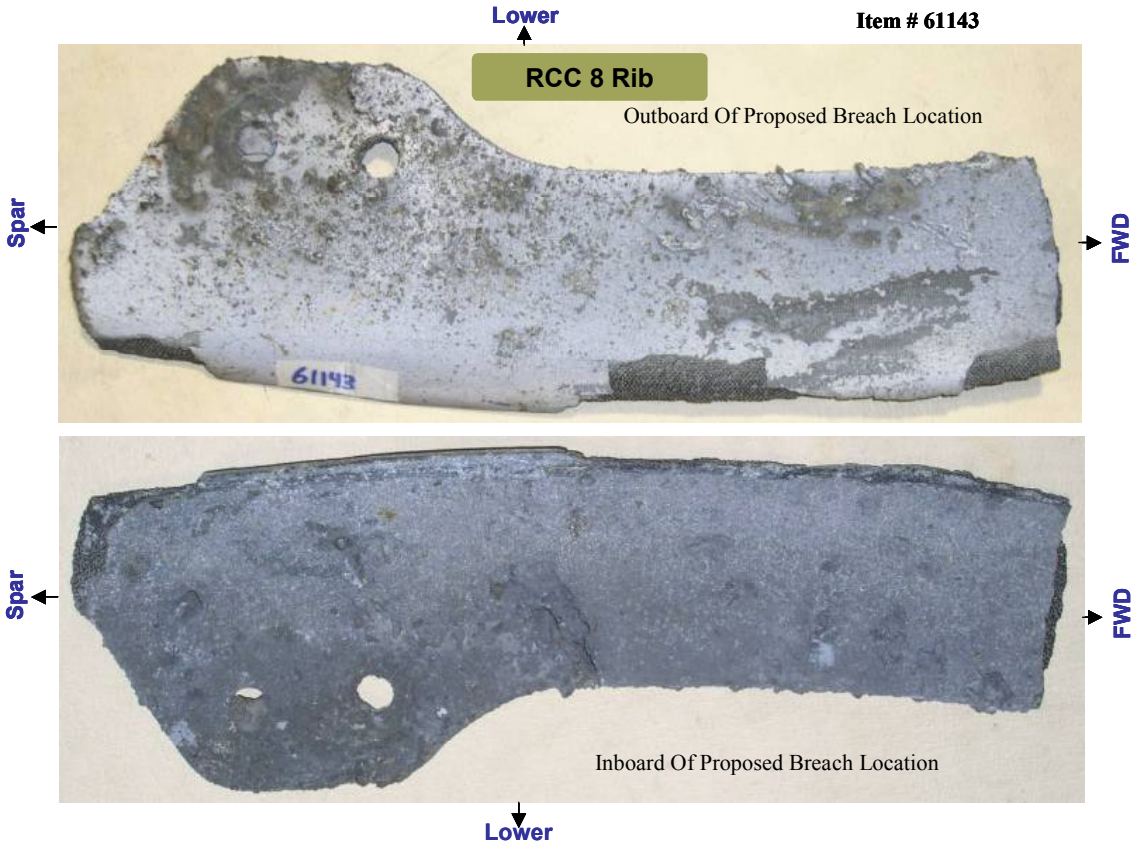

Figure 5-3. Samples of severe slag deposition on the panel 8 rib

Based on the slag deposition on the upper RCC panel 8 and the rib erosion at the panel 8/9 interface, the most likely area of damage was the bottom portion of RCC panel 8. The outboard apex on the panel 8 upper inboard rib shows knife edge erosion, and the rib tapers from a design thickness of 0.365 inches to 0.05 inches. The surface of the panel 8 outboard rib and matching heel piece show a similar sign of erosion, as does the panel 9 upper inboard rib. The erosion on both the panel 8 and 9 rib is on the inboard side, indicating that flow is coming from the panel 8 location. Additionally, several lower carrier panel tiles in the RCC panel 9 area also show significant slumping and erosion that is consistent with a hole or breach in the lower part of RCC panel 8. Figure 5-4 and Figure 5-5 show an example of the rib erosion and the flow on the lower carrier panel 9.

Figure 5-6 is a CAD drawing of the recovered debris showing overall slag deposition and erosion patterns. The drawing is a view from behind the RCC panels since this provides the best view of the erosion and slag deposition. Three full Tee seals can be seen in this drawing; the leftmost, Tee seal 9, divides panel 9 and 10; Tee seal 8 in the center divides panel 8 and 9; the rightmost, Tee seal 7, is the division between panel 7 and 8. The drawing shows the heavy slag deposition of the upper portion of panel 8 indicating that the probable breach area was the bottom of panel 8. The severely eroded RCC ribs are also visible near the RCC panel 8/9 Tee seal. The heavy slag on

these inner surfaces indicate flow from the panel 8 direction toward panel 9. This is also consistent with the knife-edge erosion shown in Figure 5-4 below. The proposed flow direction leading to the erosion and slag deposition on the lower carrier panel 9 tiles can be seen in this view as well. The detailed flow, erosion, and deposition are best viewed in Figure 5-5. The last significant feature in Figure 5-6 is the heavy slumping that is observed on the upper carrier panel 8 tile (50336T) in the upper right portion of the drawing.

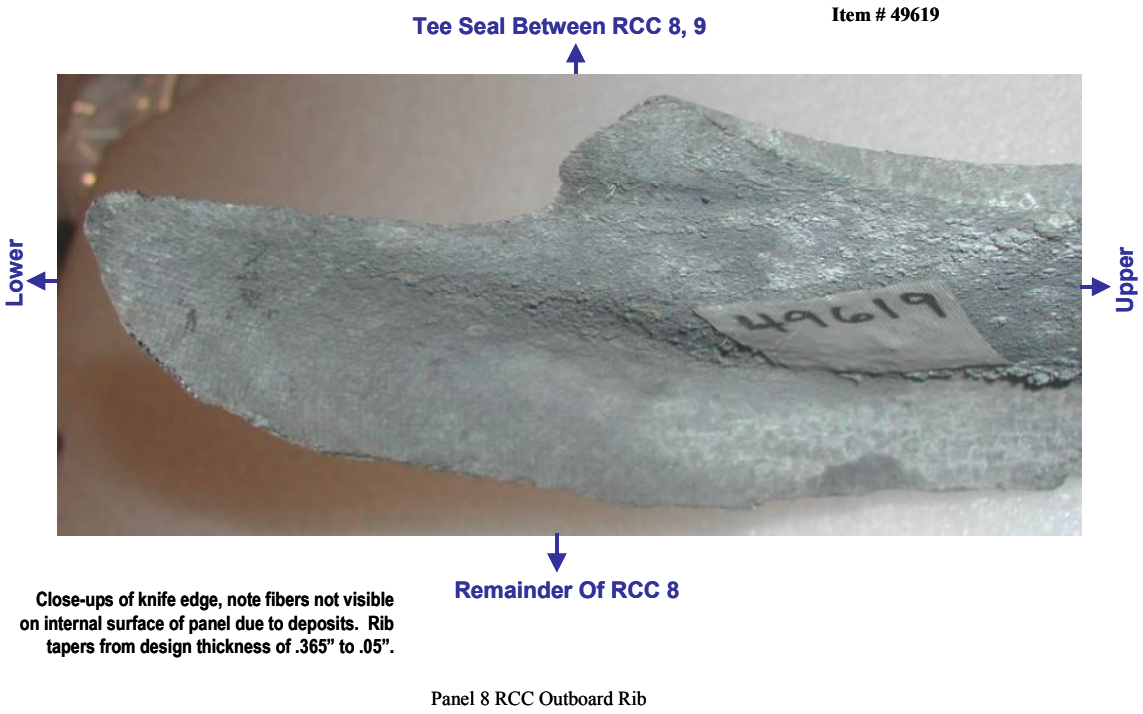

Figure 5-4. Example of rib erosion

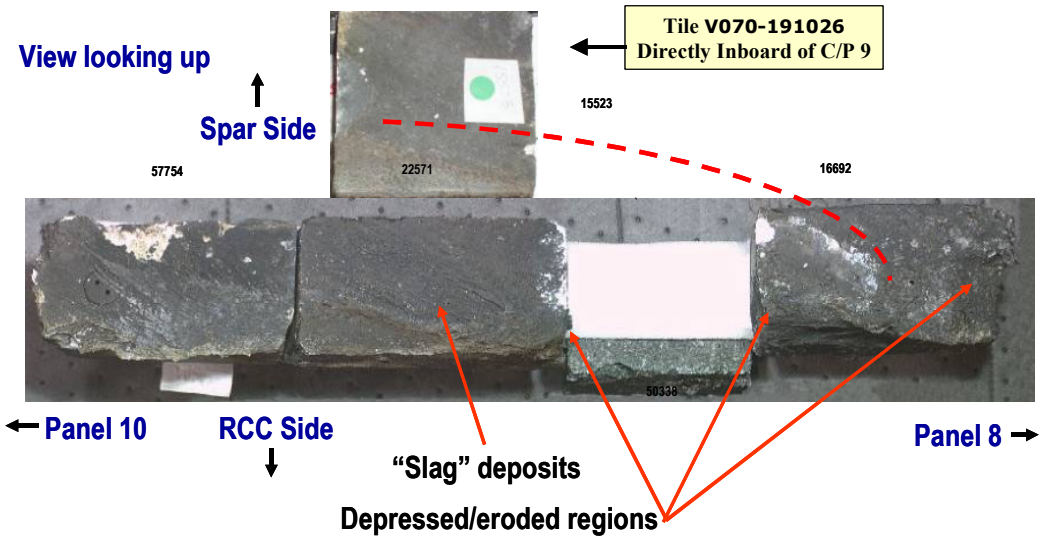

Figure 5-5. Flow on the lower carrier panel 9 tiles

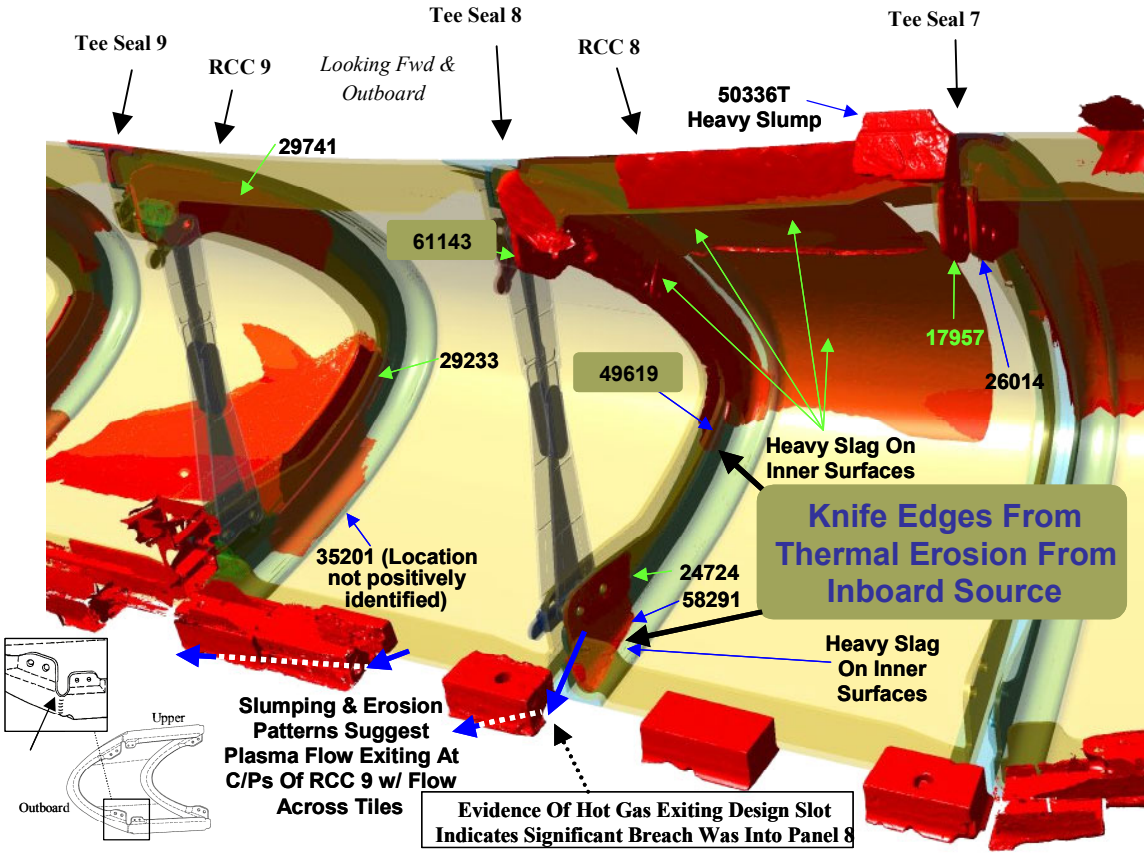

Figure 5-6. CAD drawing of the recovered debris showing overall slag deposition and erosion patterns

The data shown in Figure 5-6 is important when combined with the analysis of the slag deposition. The slag deposition on the upper RCC panel 8 was analyzed using sophisticated cross sectional optical and scanning electron microscopy, microprobe analysis, and x-ray diffraction to determine the content and layering of the slag deposition. This analysis indicated that the materials in this area were exposed to extremely high temperatures, since Cerachrome insulation was deposited first and its melting temperature is greater than 3200 degrees Fahrenheit. The analysis also showed no presence of Aluminum 286 in the slag indicating that the RCC attach fittings were not in the direct line of the breach and that the Inconel 718 spanner beam was one of the first internal items to be subjected to heating. Inconel slag was prevalent in much of the analyzed slag indicating melting of the spanner beam, foil, and associated insulation. Aluminum was found in the last deposited layer indicating the wing honeycomb spar was the last area to be subjected to hot gas flow.

Analysis of the slag deposition on the lower carrier panel 9 tiles was also performed. Materials on these tiles are consistent with wing leading edge materials (Aluminum, Inconel, Nickel Alloy, and Carbon) indicating an outflow from the panel 8 area across the tiles. Tile slumping in this area is indicative of temperatures in excess of 3000 ^{o}F. The upper carrier panel 8 tile was also analyzed and the results were similar to lower carrier panel 9 except that this tile appeared to have more Cerachrome and Nextel fiber deposits. These materials are consistent with the insulator that protects the wing leading edge spar and with flow moving toward the upper wing surface through the vent between the upper carrier panel and RCC.

This forensics analysis further corroborates the breach location to be the lower portion of RCC panel 8 below the apex, approximately midway between the apex and where the RCC panel meets the carrier panel. Based on the flow patterns, the breach was in an area that caused the flow to impact the spanner beam associated with Tee seal 8 and create the knife edge erosion shown in this area in Figure 5-6.

The flow appears to have entered through this breach and into the lower aft corner, exiting through a slot toward carrier panel 9. The flow burned through the horse collar and eroded and slumped the carrier panel tiles. The flow continually grew the hole in panel 8 as time progressed and it eroded the remaining aft flange part of RCC panel 8 and the forward flange on RCC panel 9. Although the lower carrier panel 9 tiles are slumped and eroded, there must have been an RCC rib protecting the adjacent carrier panel 8 tiles since there is no erosion or slumping of these tiles. Compared to the severely eroded carrier panel 9 tiles, the three recovered carrier panel 8 tiles are in relatively pristine condition, and likely separated due to backside heating with no indications of mechanical damage occurring prior to vehicle break-up.

As time progressed, the Cerachrome and Inconel wing spar insulators were eroded, and eventually hot gas flow impinged on the wing leading edge, burning through the honeycomb spar. Figure 5-7 depicts the possible flow direction and deposition of various metals as determined by this analysis.

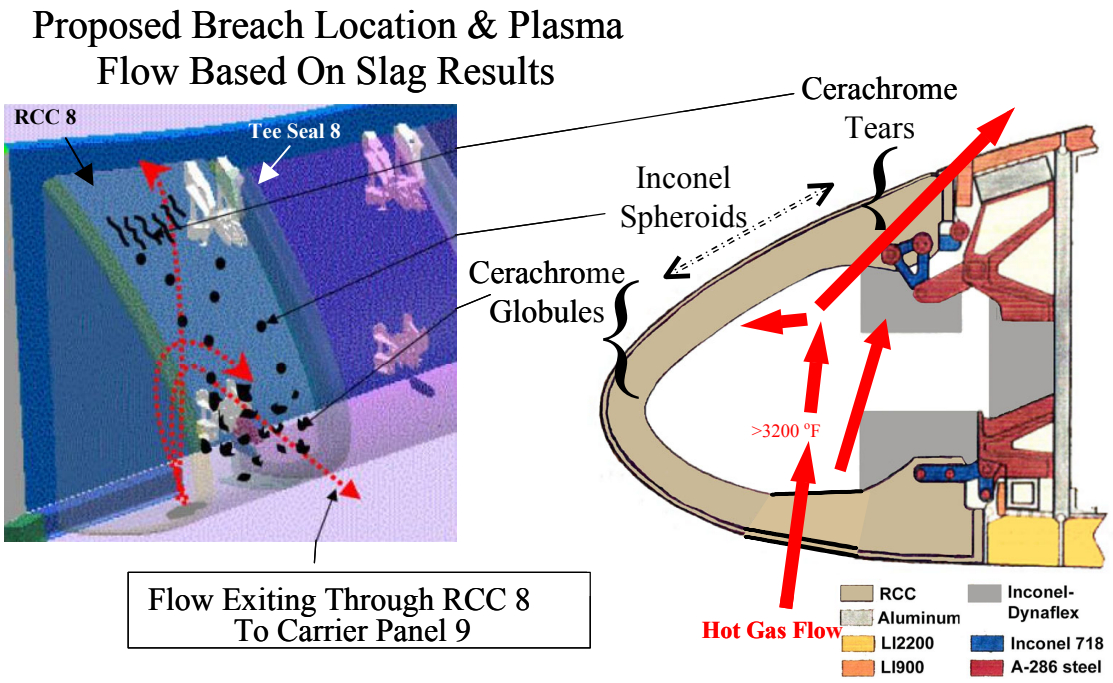

Figure 5-7. Analysis results show possible flow direction and deposition of metals

In addition to the slag deposition and flow analysis, there are two other significant pieces of data that point to a breach in the RCC 8/9 area as the initial damage. The first item is the location of the leading edge RCC in the debris footprint. Figure 5-8 shows the recovered RCC for both the left and right wing and its location in the debris footprint. The eroded RCC pieces from panels 8 and 9 are found in the westernmost part of this debris footprint near Waxahachie, Texas, along with other pieces of RCC panel 8. Left wing RCC panel 9 and other aft panels appear to have been lost relatively early in the break-up sequence since their footprint spans the western to center part of the footprint. This is indicative of a left wing breach in the panel 8/9 area. The forward portion of the RCC panels on both the left and right wings (panels 1 through 7) are found from the center to eastern part of the debris footprint possibly indicating that these were lost in a secondary aerodynamic break-up.

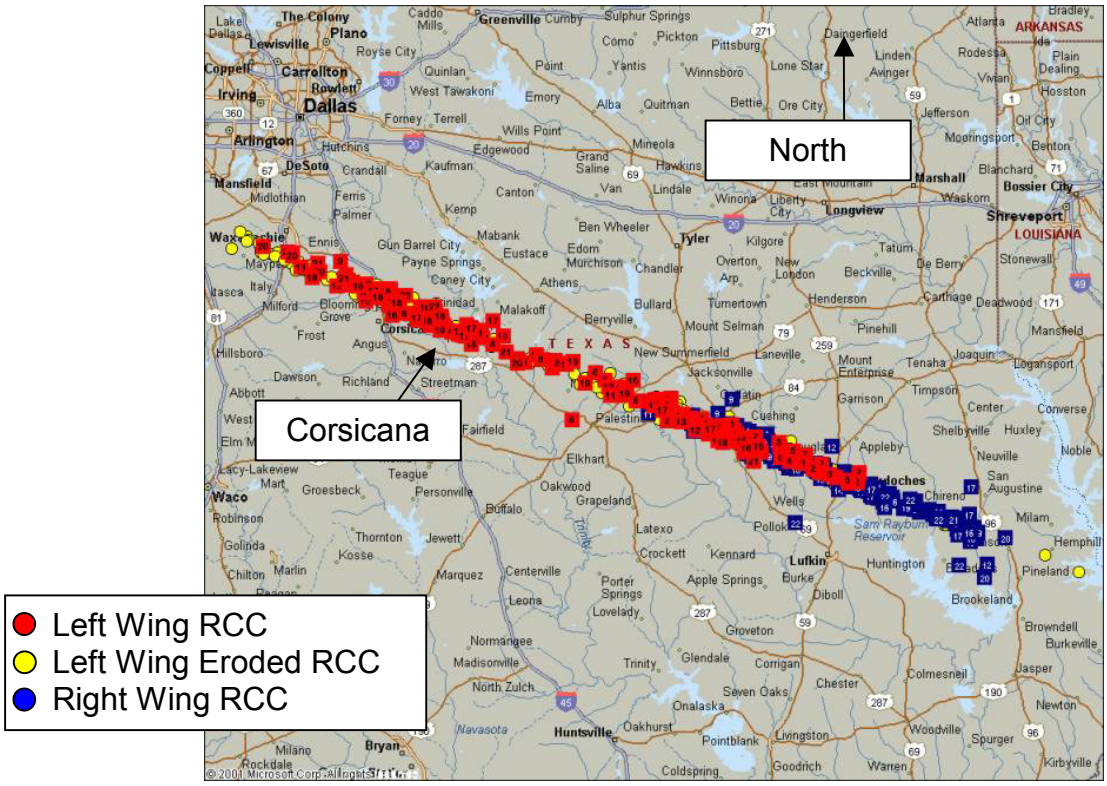

Figure 5-8. RCC panel debris location

The second additional piece of data is an upper left wing tile recovered near Littlefield, Texas. Littlefield is a small town near the Texas/New Mexico border along Columbia's ground track. This tile is the westernmost piece of debris that has been found to date in the debris recovery efforts. Due to the unique features of the tile (thickness, shape, paint, etc.), the tile must be from the upper wing area in the RCC panel 9 area. Figure 5-9 shows the only three possible locations for this tile.

The tile departed the orbiter more than one minute prior to final break-up due to prolonged internal heating of the upper wing skin in the area shown in Figure 5-9. The tile shows indications of backside heating and an RTV debond. It was not a failure in the densification layer, which would have been caused by mechanical loading. This piece of recovered debris is not very significant on its own merit; however, it is consistent with the previously discussed forensics data (rib erosion, carrier panel 9 tile slumping, etc.) and other events that will be discussed later in Section 5.4.

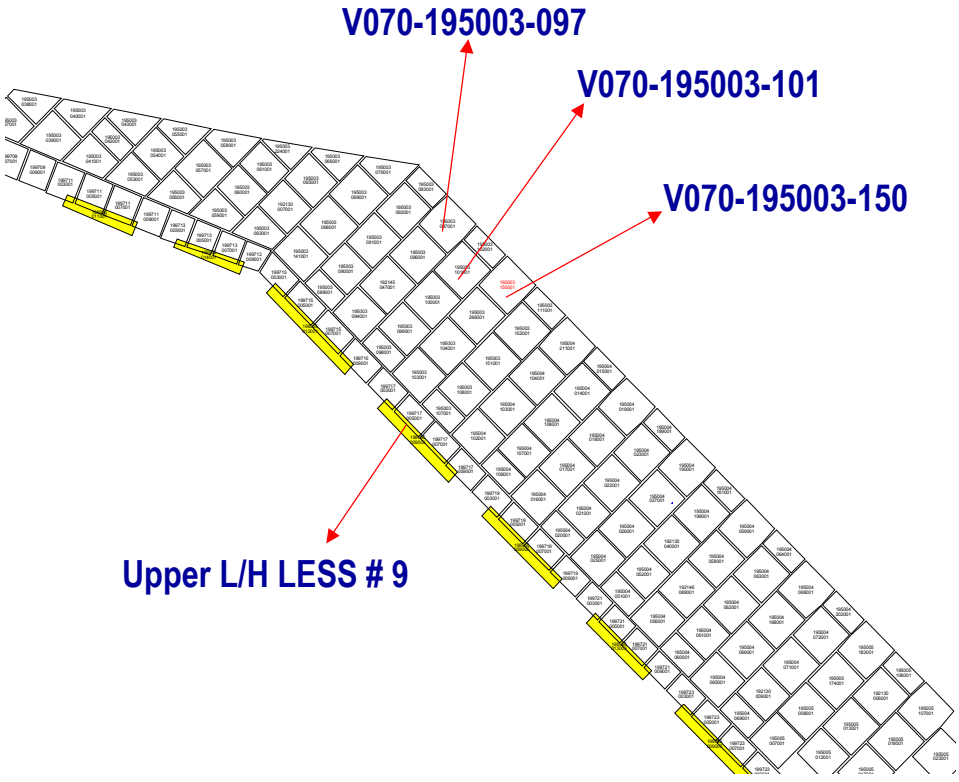

Figure 5-9. Three possible orbiter locations of the Littlefield tile on left wing

5.4 ENTRY EVENTS TIMELINE

5.4.1 Early Entry Heating Events

Columbia successfully completed the deorbit burn at 8:18:08 EST over the Indian Ocean. The deorbit burn and entry targeting were accomplished using well-established Mission Control Center procedures, and there were no problems identified with this process. Both the left and right Orbital Maneuvering System (OMS) engines performed nominally and the post burn residuals were less than 0.2 feet per second indicating a precise burn. The maneuver to the Entry Interface (EI) attitude, the Forward Reaction Control System Dump, and remaining Auxiliary Power Unit (APU) start (APU 1 and APU 3) were accomplished nominally.

At 8:44:09 EST, Columbia reached EI, the transition between orbital and atmospheric flight. The altitude was 400,000 feet and the orbiter was traveling Mach 24.6 in wings level (zero degree bank) attitude with a nominal 40-degree angle of attack. The orbiter guidance had been moded to OPS 304 nominally at five minutes prior to entry interface. OPS 304 is the name given to the entry flight software that contains the aerojet digital auto-pilot control mode. It is used from five minutes prior to EI through Mach 2.5. Figure 5-10 is a plot of dynamic pressure and stagnation heating from EI to vehicle break-up. The plot shows that both heating and dynamic pressure were very low during the two to three minutes (120-180 seconds) after EI. The heating rate shown is stagnation heat flux that is the allowable heat flux that could be achieved by the gas if all its thermal and kinetic energy were available. For this plot and others that follow in Section 5, EI occurred at 8:44:09 EST, which corresponds to zero seconds on the plots. This is a convenient reference point for many of the entry events that will be discussed.

At approximately 8:48:39 EST (EI + 270 sec.), a left wing leading edge spar strain gauge began a small off-nominal increase. Figure 5-11 shows the STS-107 response of this strain measurement along with three other previous Columbia missions. Figure 5-12 shows the location of this sensor (WLE Strain V12G9921) and others on the wing leading edge. The damage in lower RCC panel 8 is believed to be the cause of this strain increase. The breach allowed hot gas intrusion onto the panels 8 through 9 wing leading edge spar area leading to extreme heating and thermally induced strain. The strain increase grew over time and reached a maximum at approximately 8:50:09 EST (EI + 360 sec.). Thermal and structural analyses indicate that a breach would need to be within approximately 15 inches of the strain gauge to create the observed strain increase.

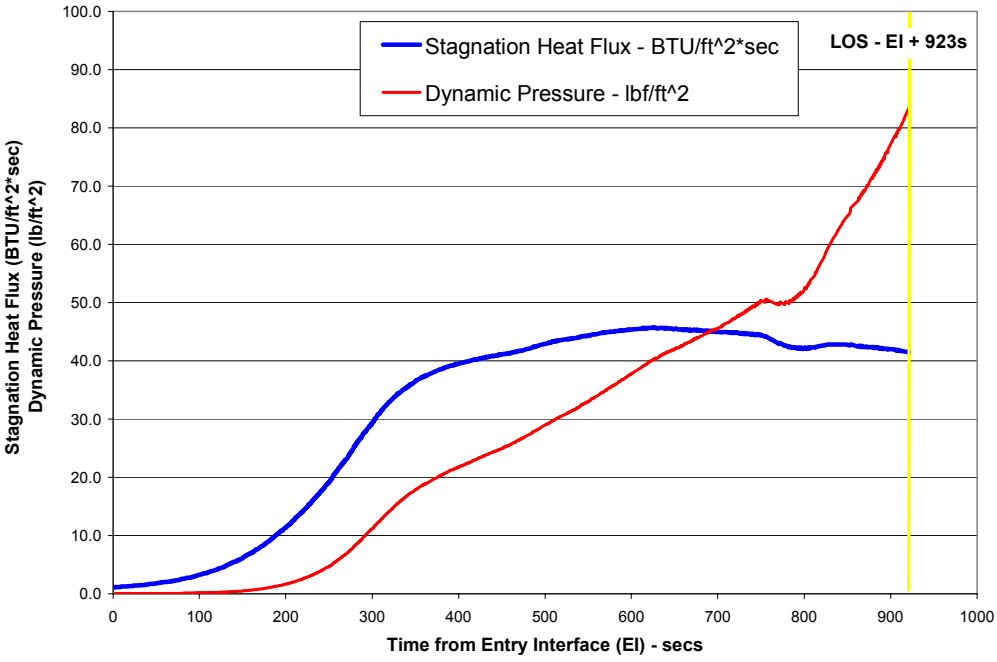

Figure 5-10. STS-107 stagnation heat flux and dynamic pressure. Note that EI was at 8:44:09 EST.

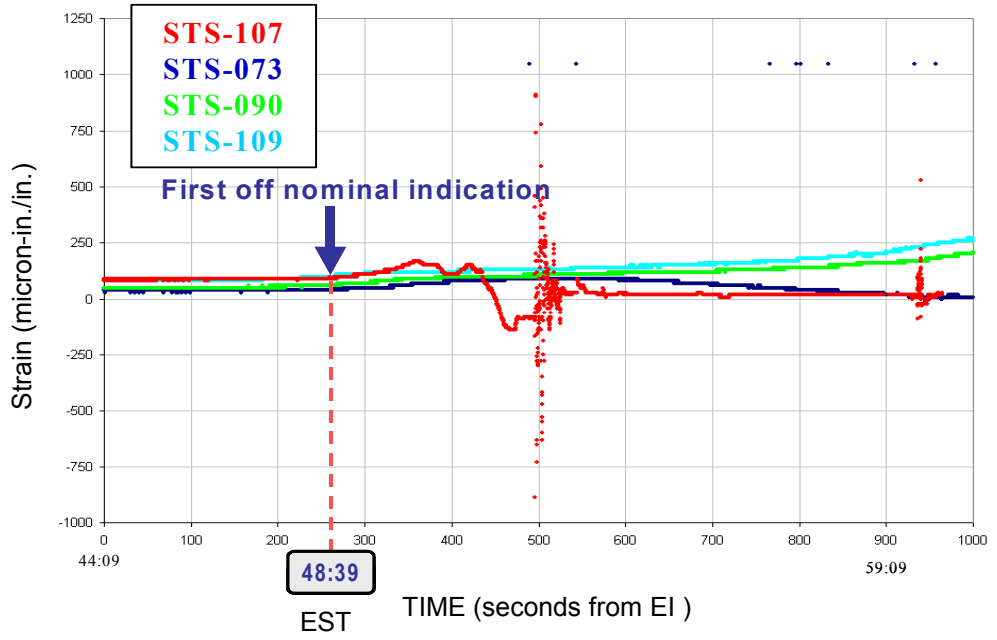

Figure 5-11. Left wing RCC panel 9 strain gauge is first measurement to indicate an off-nominal event. Note that EI was at 8:44:09 EST.

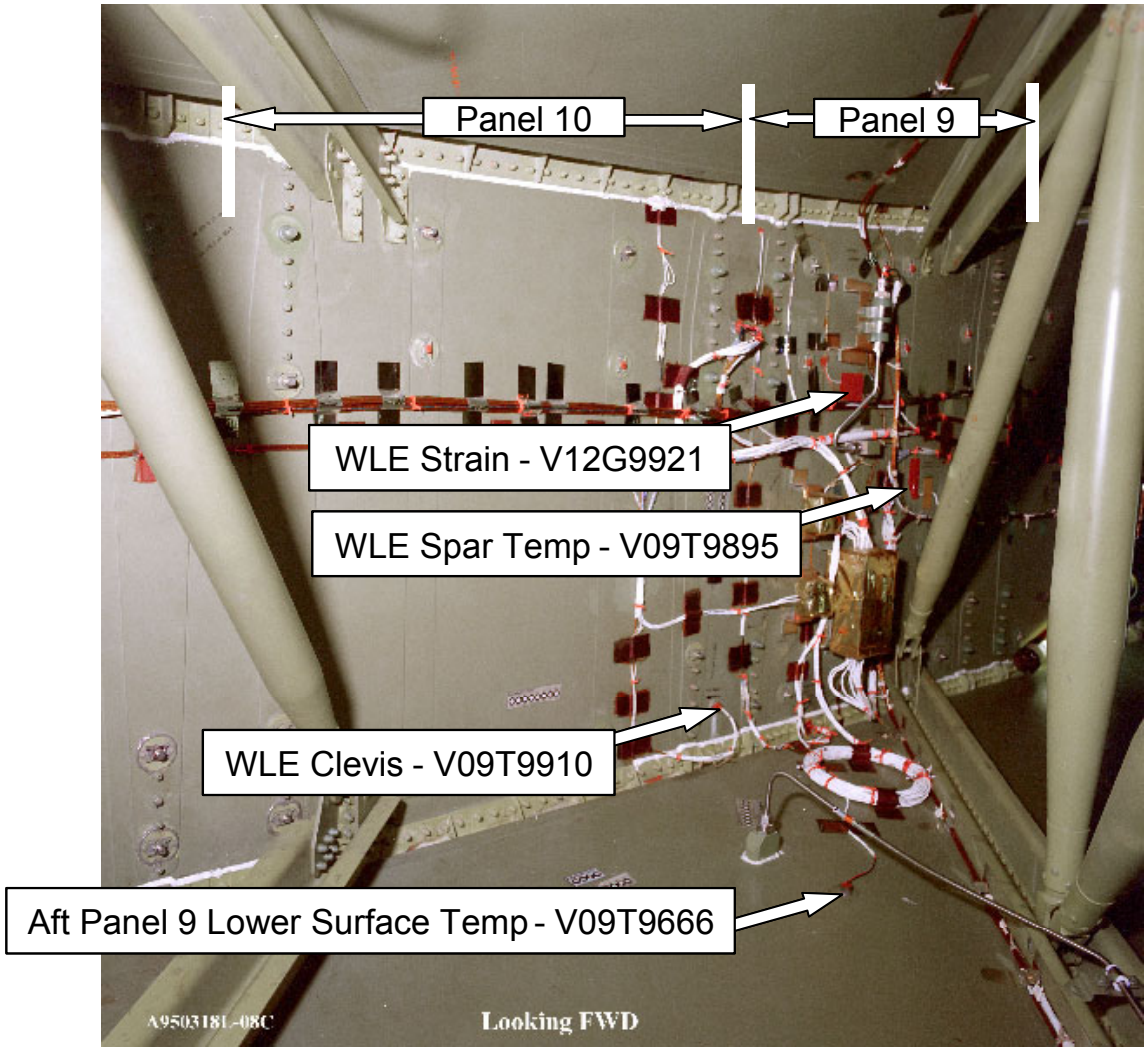

Figure 5-12. MADS sensors inside left wing

Twenty seconds later at 8:48:59 EST (EI + 290 sec.), the left wing lower attach clevis temperature sensor (between RCC panel 9 and 10) began an early off nominal temperature trend. Figure 5-13 shows the abnormal temperature response when compared to other Columbia missions. This temperature rise is consistent with an early entry of hot gas into the RCC cavity. This Modular Auxiliary Data System (MADS) measurement (V09T9910) is the only temperature measurement located in the RCC cavity along the left wing leading edge. It is positioned on the lower attach fitting between panel 9 and 10 and is well protected thermally by Inconel foil insulation. The sensor is also thermally isolated since it sits on the attach fitting away from other structure as shown in Figure 3-15. In order to get an early temperature rise for this sensor, unlike that observed on any other flight, there must be a path in the RCC cavity to allow hot gas to reach the sensor.

A thermal analysis was performed with heating rates from various hole sizes in the bottom of RCC panel 8 in an attempt to match this temperature rise. The analysis used a thermal math model of the wing leading edge (Inconel Cerachrome insulation, Inconel 718 and A-286 steel attach fittings, and aluminum honeycomb spar). The results indicated that the heating equivalent of a 6 to 10 inch diameter hole with a 10 percent "sneak flow" around the insulation would be required to match the thermal response of the clevis temperature. In the same timeframe several MADS lower surface temperatures on the left wing showed a slight off nominal early temperature rise when compared to previous flights of Columbia of the same inclination.

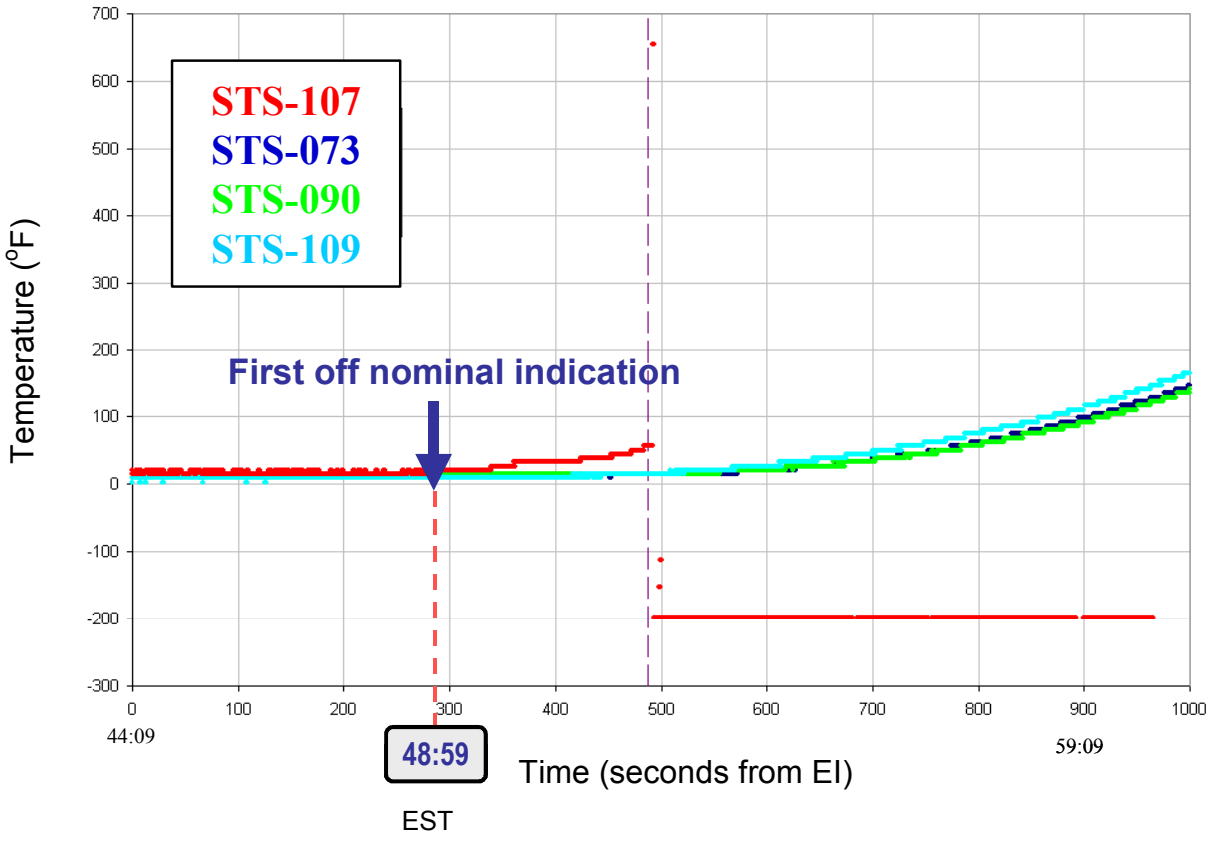

Figure 5-13. Left wing RCC panel 9/10 clevis temp sensor is second measurement to indicate an off-nominal event

5.4.2 First Roll Maneuver Through Wing Spar Breach

Columbia executed a nominal roll to the right at 8:49:32 EST (EI + 323 sec.) as the entry guidance software began to actively control energy (i.e., closed loop guidance) to land at KSC. This initial roll command is also timed to ensure atmospheric capture by reducing the lift on the vehicle. Within 17 seconds of this maneuver, at 8:49:49 EST (EI + 340 sec.), four left OMS pod surface temperature measurements showed an off-nominal trend with lower temperature rises when compared to similar Columbia missions. A sample of these measurements compared to other Columbia missions is shown in Figure 5-14, and the location of these measurements on the left OMS pod forward face can be found in Figure 5-15.

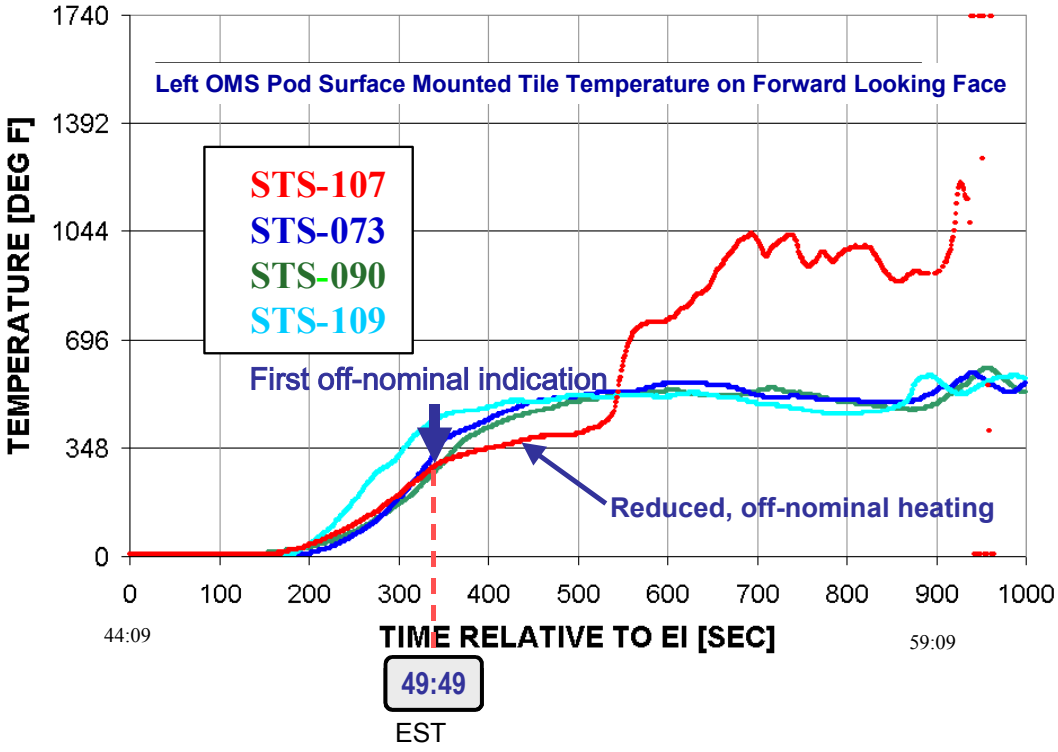

Figure 5-14. Typical off-nominal OMS pod thermocouple (V07T9220A)

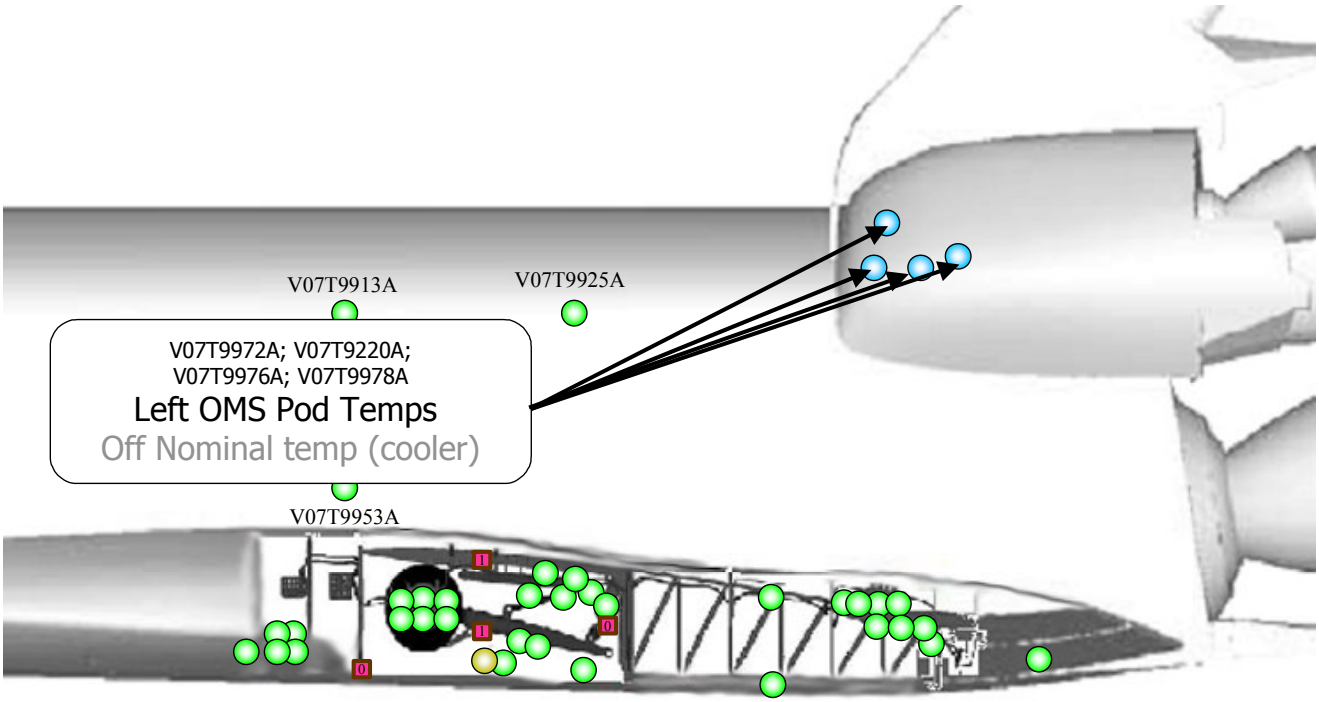

Figure 5-15. Location of OMS pod thermocouples off-nominal low

The reduced heating is not completely understood since the weak aerodynamic flow field on the upper surface of the orbiter is difficult to model and is extremely sensitive to disturbances. The best explanation for this reduced heating is that flow into the RCC cavity was venting through to the upper surface of the wing through an existing 0.1-inch vent between the RCC and upper surface carrier panels. This vent exists all along the leading edge from RCC panel 1 through panel 22 and has an approximate area of 66 square inches. This upper surface RCC venting and the flow disturbance created by the panel 8 and upper carrier panel 8 damage caused the vortices from the canopy or area where the wing meets the orbiter fuselage to move from their normal positions, thus reducing the heating on the OMS pod. Figure 5-16 depicts the change in the upper wing surface vortices and the weak upper surface flow.

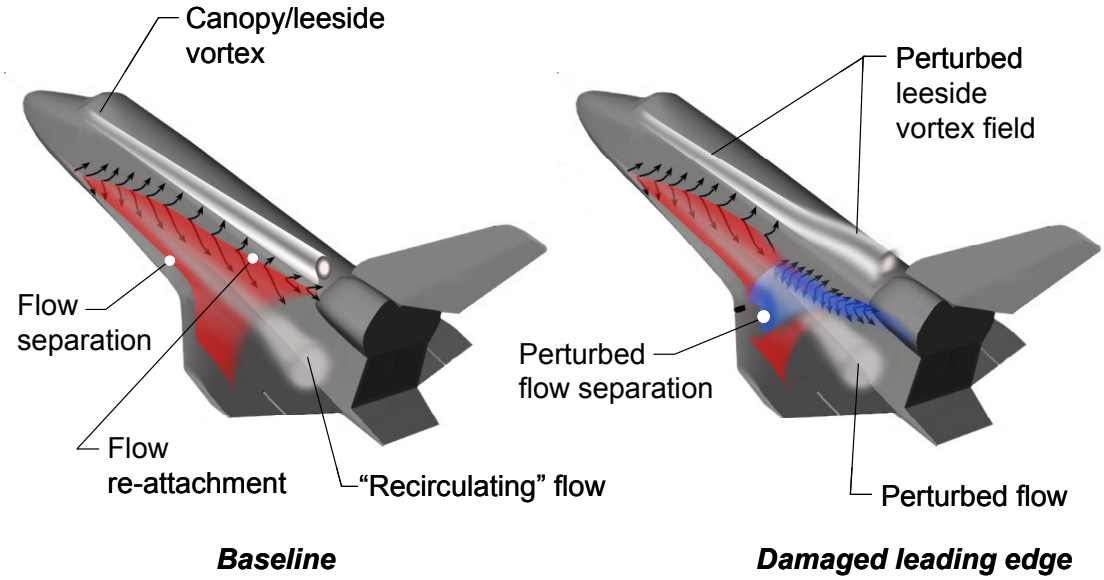

Wing leading edge damage perturbs leeward flow separation and re-attachment locations as well as leeward embedded shocks (not shown)

Figure 5-16. Postulated orbiter leeside flow field associated with wing leading edge damage

In order to verify this theory of a weak upper surface flow being disturbed from venting on the upper surface, several wind tunnel tests were performed in the NASA Langley Research Center Mach 6 Tetraflouromethane (CF4) Wind Tunnel. The use of CF4 as the gas for the flow analysis is required to best replicate the Mach number environment during this timeframe. These wind tunnel tests used a ceramic model and a 0.01-inch leading edge vent to mimic the postulated venting. Nitrogen gas was allowed to flow through this upper surface vent via a gas supply line. A picture of this model is shown in Figure 5-17. Results of this testing show that it is feasible to obtain reduced heating on both the left OMS pod and the left fuselage as a result of flow through the RCC upper surface vent. Figure 5-18 shows the change in heating as the vent velocity is altered.

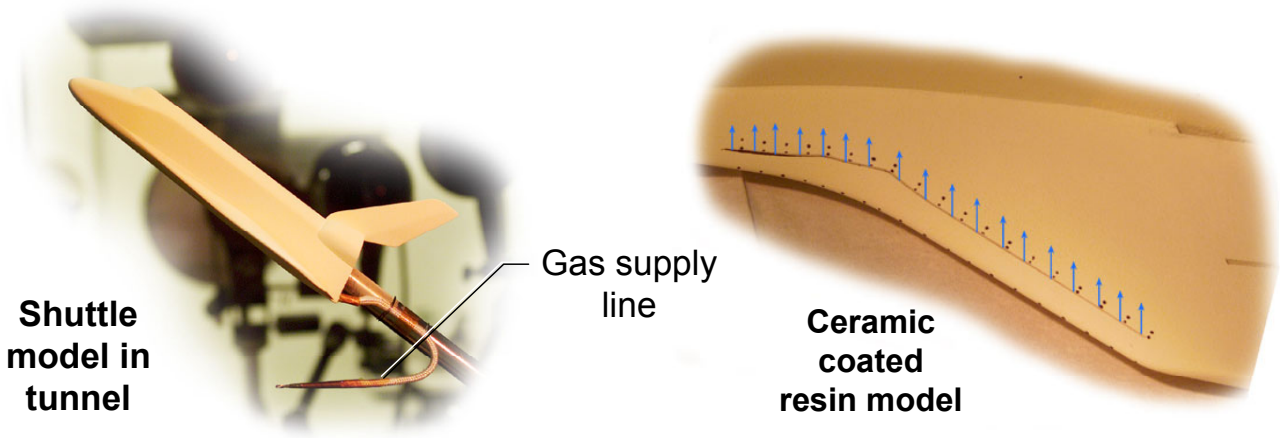

Figure 5-17. Orbiter wind tunnel model with vent gap along wing leading edge

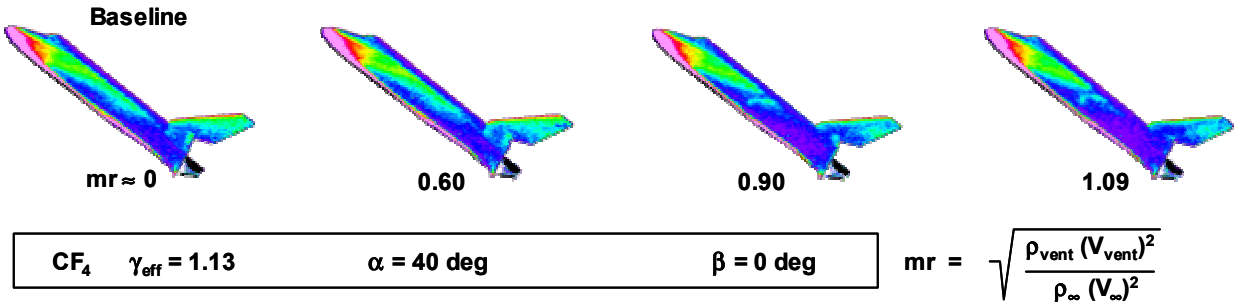

Figure 5-18. Wind tunnel model results for sensitivity of orbiter side fuselage and OMS pod heating patterns to mass addition along WLE leeside vent gap

Over the next 43 seconds, there were five communications dropouts beginning at 8:50:00 EST and ending at 8:50:43 EST (EI + 351 through 394 sec.). It is possible that hot gas in the RCC cavity had begun to erode the Inconel and Cerachrome insulation along the wing leading edge spar. Molten materials could have been ejected into the environment around the orbiter creating multi-path signal scattering with the link between the orbiter and the western Tracking and Data Relay Satellite (TDRS). The best parallel for this explanation is chaff used by some military aircraft to confuse opposing radar systems.

Forensic analysis of the recovered left OMS pod debris indicates that molten Inconel 718 and A-286 cress were sprayed onto the left OMS pod during entry. This OMS pod debris and the left side of a recovered vertical tail debris piece were significantly pitted by this metallic spray supporting the concept that there was vaporized metal in the environment around Columbia. These materials must have originated from the RCC panel 8 wing spar damage area since Inconel 718 is used as the wing leading edge insulator and A-286 is used for the RCC attach fittings.

In the same timeframe, at 8:50:09 EST (EI + 360 sec.), a left payload bay fuselage MADS surface temperature measurement (Figure 5-19) showed an off-nominal temperature trend. This trend is a reduced rise rate when compared to other previous Columbia missions, as shown in Figure 5-20. The previously discussed theory of venting and or disturbed flow due to panel 8 damage, causing a shift in the vortices on the upper surface of the wing, is also believed to be the cause of this off-nominal behavior. The flow field and venting on the upper surface rate are constantly increasing since the mass flow rate into the RCC breach is increasing as the orbiter descends lower into the atmosphere.

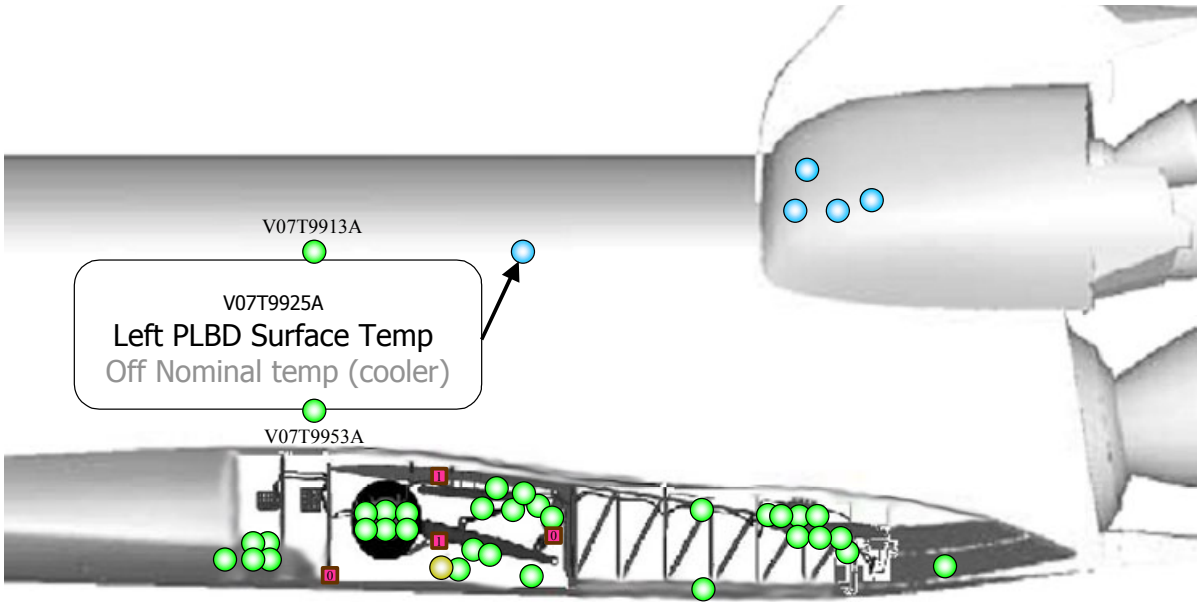

Figure 5-19. Location of left sidewall temperature sensor

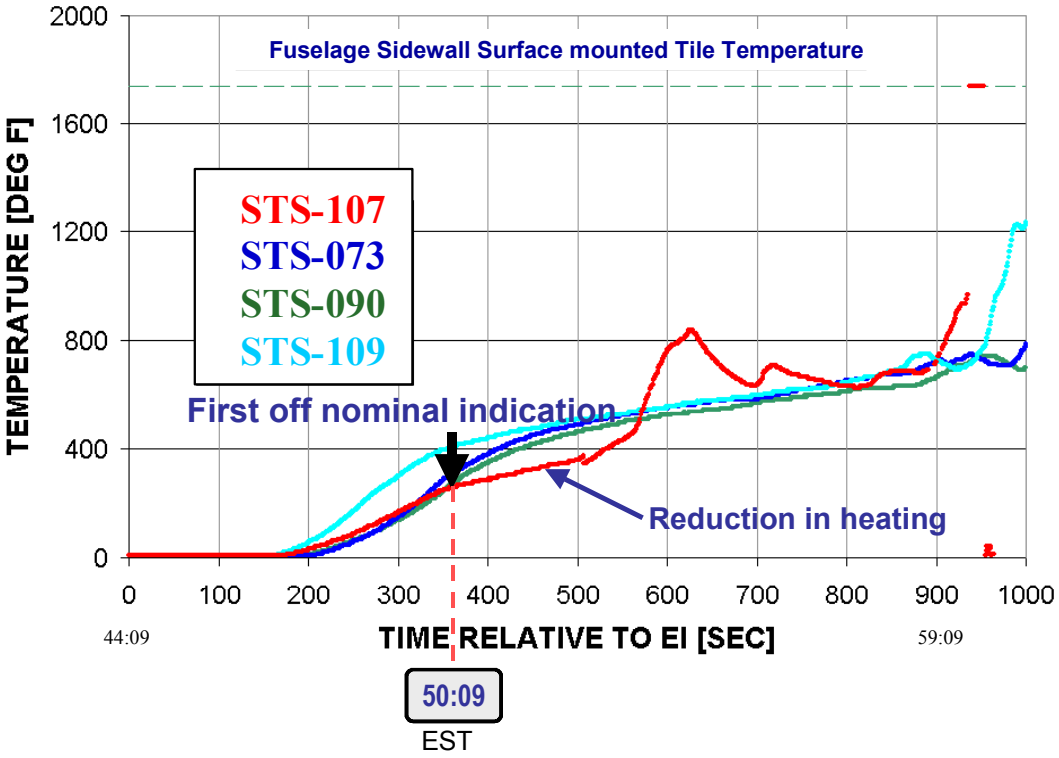

Figure 5-20. Off-nominal temperature indication on the left sidewall

At 8:50:19 EST (EI + 370 sec.), a lower surface thermocouple showed signs of off nominal, increased heating. The best explanation for the increased heating in this area is severely disturbed, turbulent flow caused by the leading edge damage on the bottom of RCC panel 8 and flow from the lower corner of this panel as discussed in Section 5.3. Langley Research Center wind tunnel testing has confirmed that wing leading edge damage (notch or protuberance) near panel 8 will cause increased heating to the lower wing surface. As previously discussed, the eroded lower carrier panel tiles on panel 9 indicate this strong flow from panel 8. This is consistent with flow patterns observed on many recovered lower surface wing acreage tiles along the flow lines aft of the RCC panel 8 area. Figure 5-21 shows this temperature response as compared to other Columbia missions. The location of the sensor can be seen in Figure 5-22.

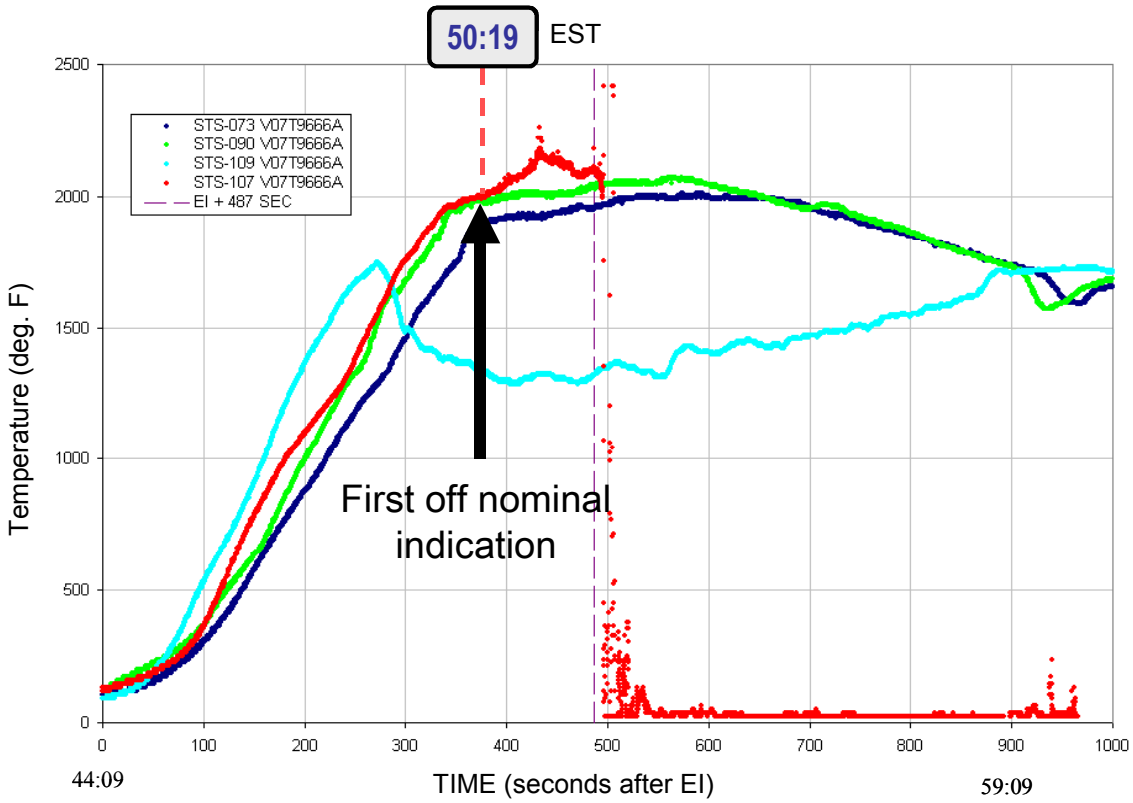

Figure 5-21. Temperature rise on tile surfaces aft of RCC panel 9

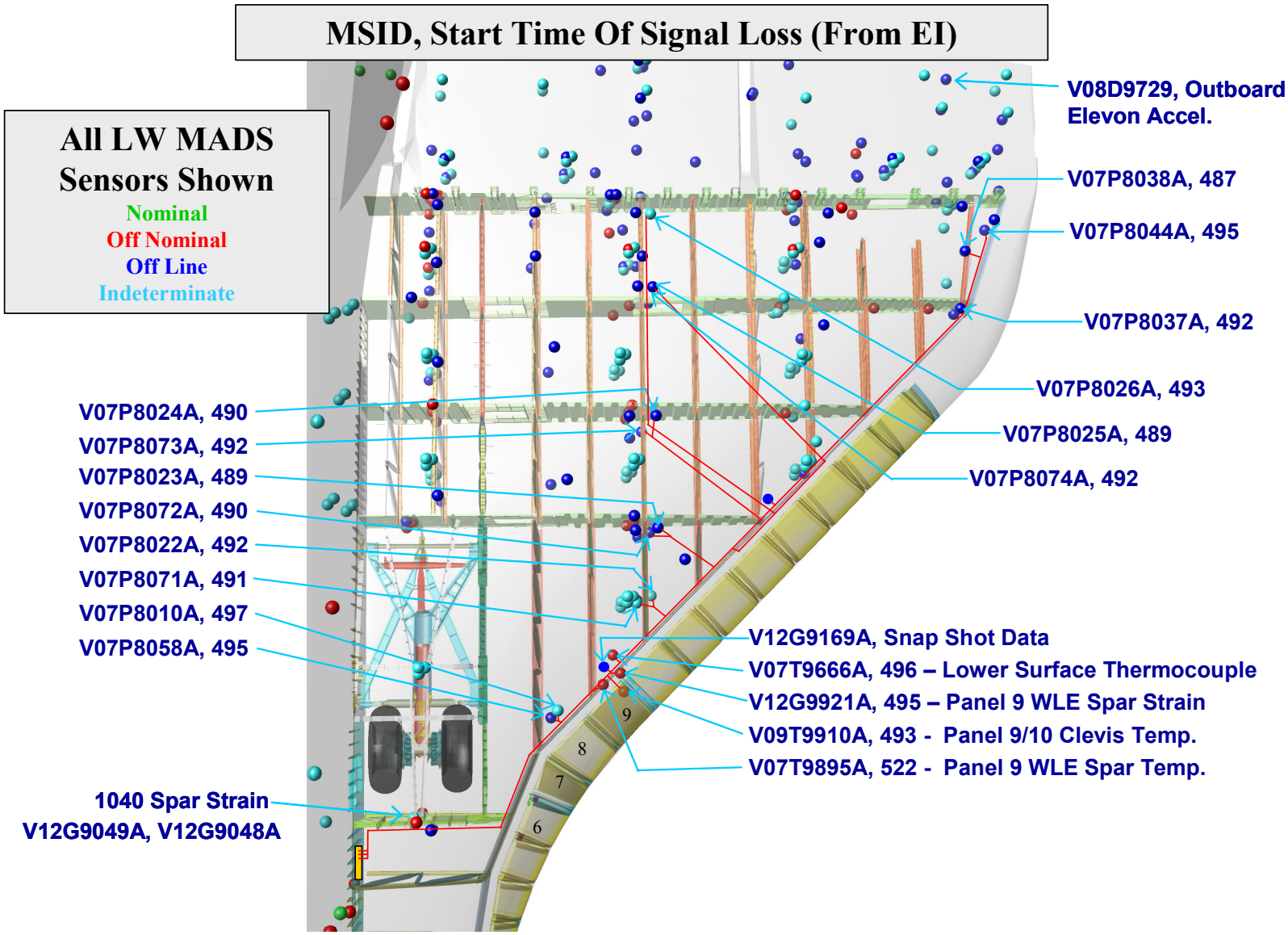

Figure 5-22. Left wing MADS sensors, including Measurement Stimulation Identification (MSID) number, and start time of loss of signal (EI + sec.)

By 8:51:14 EST (EI + 425 sec.), the wing leading edge spar temperature began an early, off-nominal rise, shown in Figure 5-23. At the same time, the clevis temperature in the RCC panel 9/10 region continued to increase. The initial spar temperature rise was relatively slow and was caused by conduction since this measurement is on the backside of the spar in the wing cavity. Eventually, the rise rate increased dramatically as first the Inconel and Cerachrome insulation and later the aluminum honeycomb were destroyed. The exact time of the spar breach is unknown; however, it is estimated to have occurred between 8:51:14 to 8:51:59 EST (EI + 425 to 470 sec.) based on the observed wing leading edge linear decrease in strain during this timeframe. A more detailed discussion of the method used to bracket the time of the wing spar breach is contained in the following section.

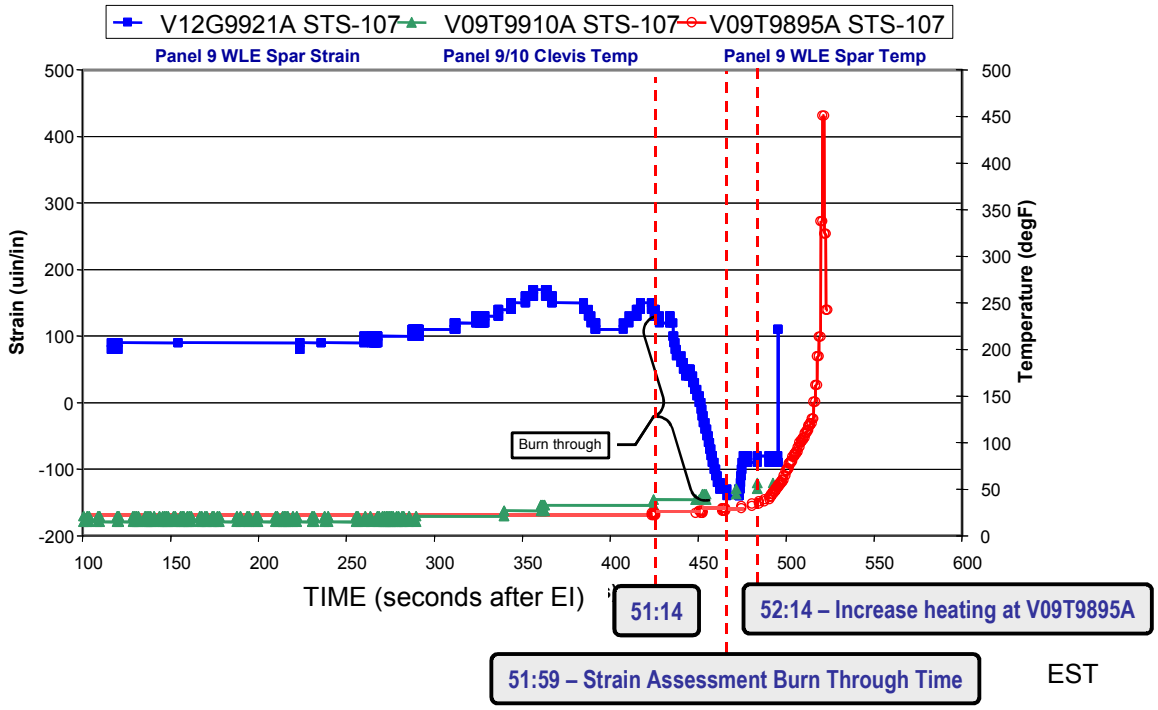

Figure 5-23. RCC panel 9 MADS strain and temperature measurements, STS-107

At 8:51:49 EST (EI + 460 sec.), one of the left OMS pod measurements (V07T9972A) began to show an increased temperature rise, indicating that the upper surface flow has changed again. This is shown in Figure 5-24 along with this measurement on other Columbia missions. It is evident that the measurement rises to a higher temperature and at a faster rate than has been observed on previous missions within the next few minutes. Figure 5-25 shows other left OMS pod and fuselage temperature measurements that exhibit an off-nominal rise later in time. The sensor locations on the left side of the orbiter are also shown in Figure 5-25.

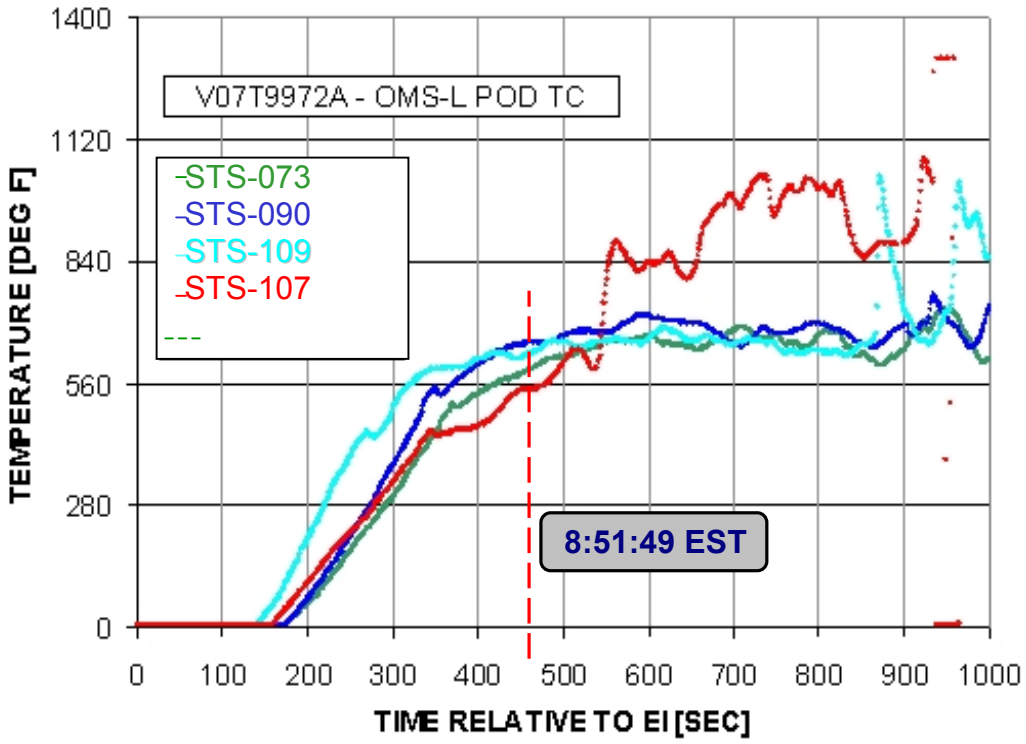

Figure 5-24. Off-nominal low OMS pod thermocouple (V07T9972A)

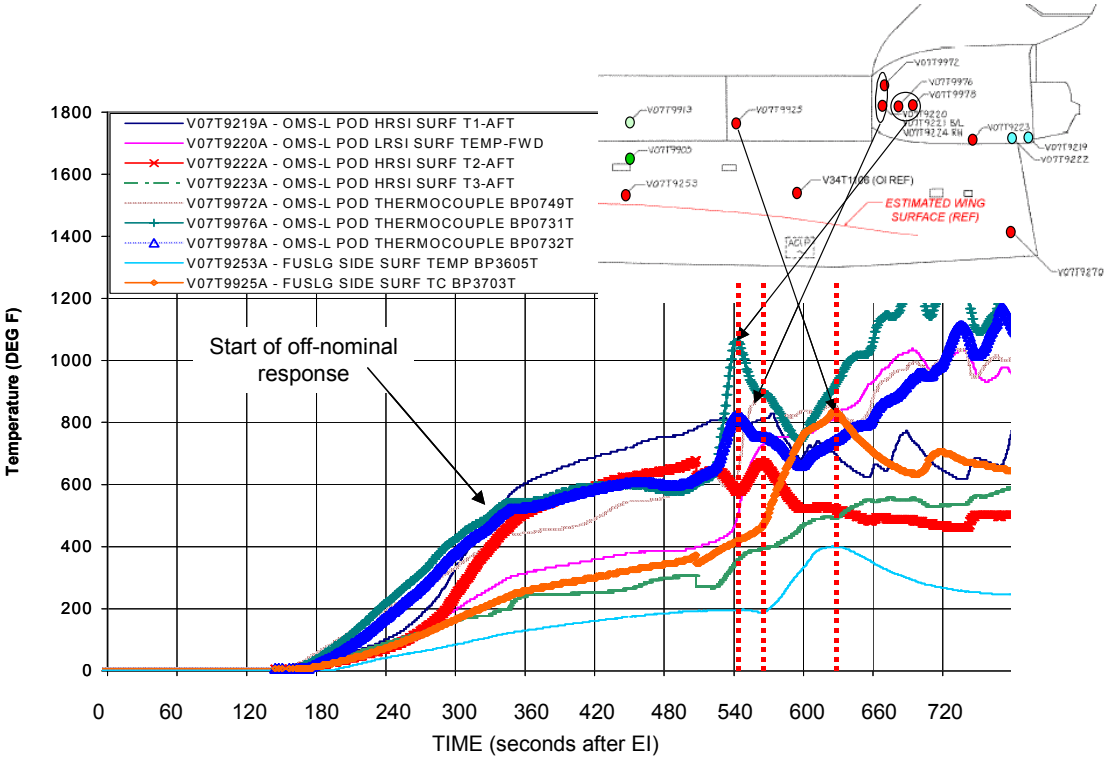

Figure 5-25. Left side fuselage/OMS pod off-nominal responses indicate increased heating

These off-nominal temperature rises were caused by a change in the flow field along the upper portion of the left wing as the wing leading edge (WLE) and wing spar damage progressed. The mechanism was a shift in the vortices due to venting on the upper portion of the wing and is similar to the previous discussions on lower than expected OMS pod temperatures. Wind tunnel testing and CFD analysis confirmed that WLE damage on RCC panels 8 and 9 could cause increased heating to the OMS pod due to disturbed upper surface flow or flow impingement caused by re-directed flow from the lower surface. Additionally, the molten Inconel 718 and A-286 spray onto this area are indications that this flow is the cause of these temperature rises. Figure 5-26 (from wind tunnel test results) is a representative example of increased heating on the left fuselage and OMS pod due to RCC panel 9 damage from wind tunnel test results. Figure 5-27 shows a similar picture of the left side as determined by CFD analysis. Note that neither the wind tunnel testing nor the CFD analysis accounts for increased heating that is likely due to molten metal contacting the OMS pod.

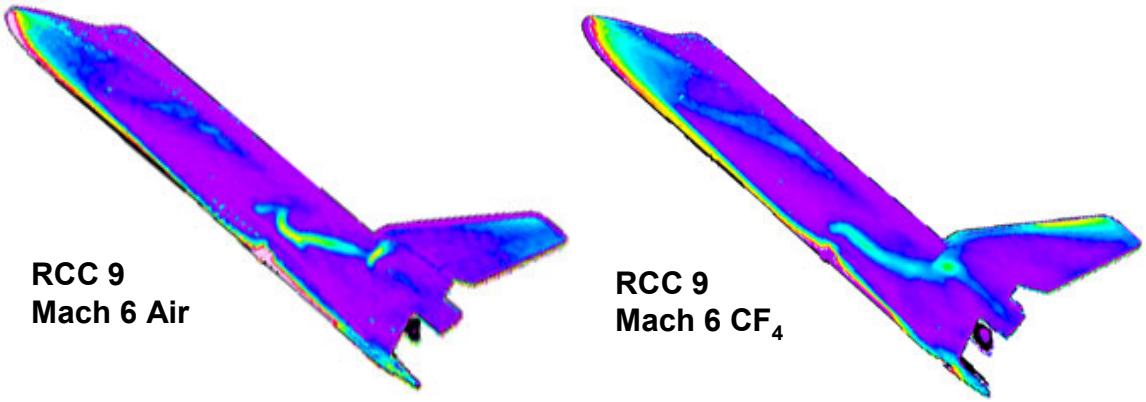

Figure 5-26. Wing tunnel test results for RCC panel 9 missing and resulting in increased heating to OMS pod

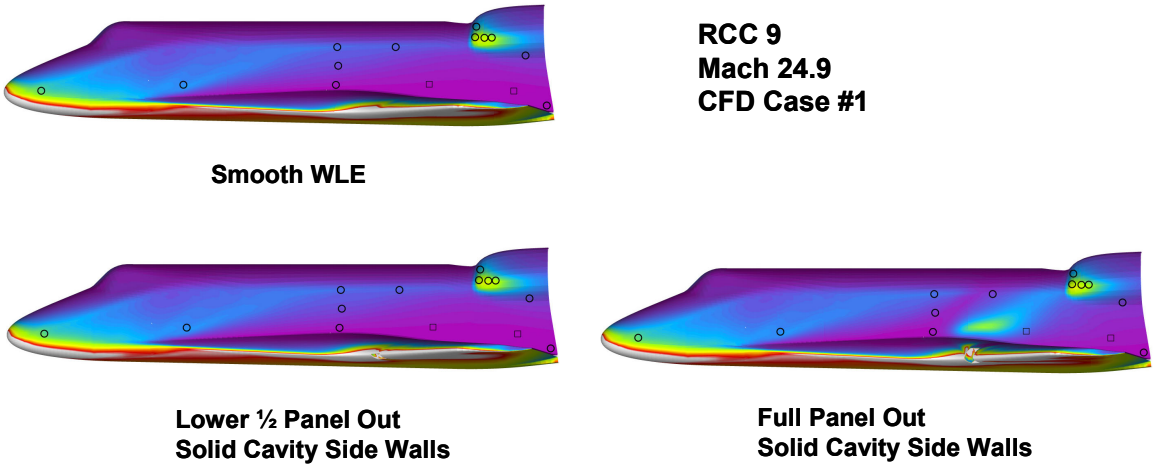

Figure 5-27. CFD results for no damage, partial damage, and full damage to RCC panel 9 show increased heating on side fuselage and OMS pod

The increased heating implies that damage/erosion to the RCC panel 8 area had increased or that at least one carrier panel had been lost. The increased heating is also consistent with an increased mass flow rate due to the nature of the entry environment. The dynamic pressure and stagnation heat flux had more than doubled by this timeframe when compared to a few minutes after EI. There are three additional communication dropouts that follow at approximately 8:52:09 EST to 8:52:31 EST (EI + 480 to 502 sec.). Again, these dropouts are consistent with molten aluminum and other metals being released into the environment surrounding Columbia.

5.4.3 Wing Breach and Wire Failures

The next significant event was a breach through the left wing leading edge spar leading to many wire measurement failures and eventual deformation of the left wing. As discussed in Section 5.4.2, by approximately 8:52:00 EST (EI + 471 seconds), strain and temperature measurements indicated that hot gas had begun to weaken the wing spar. Figure 5-28 shows that the orbiter has entered the peak-heating region during this timeframe and would remain there for many of the ensuing events that will be discussed later.

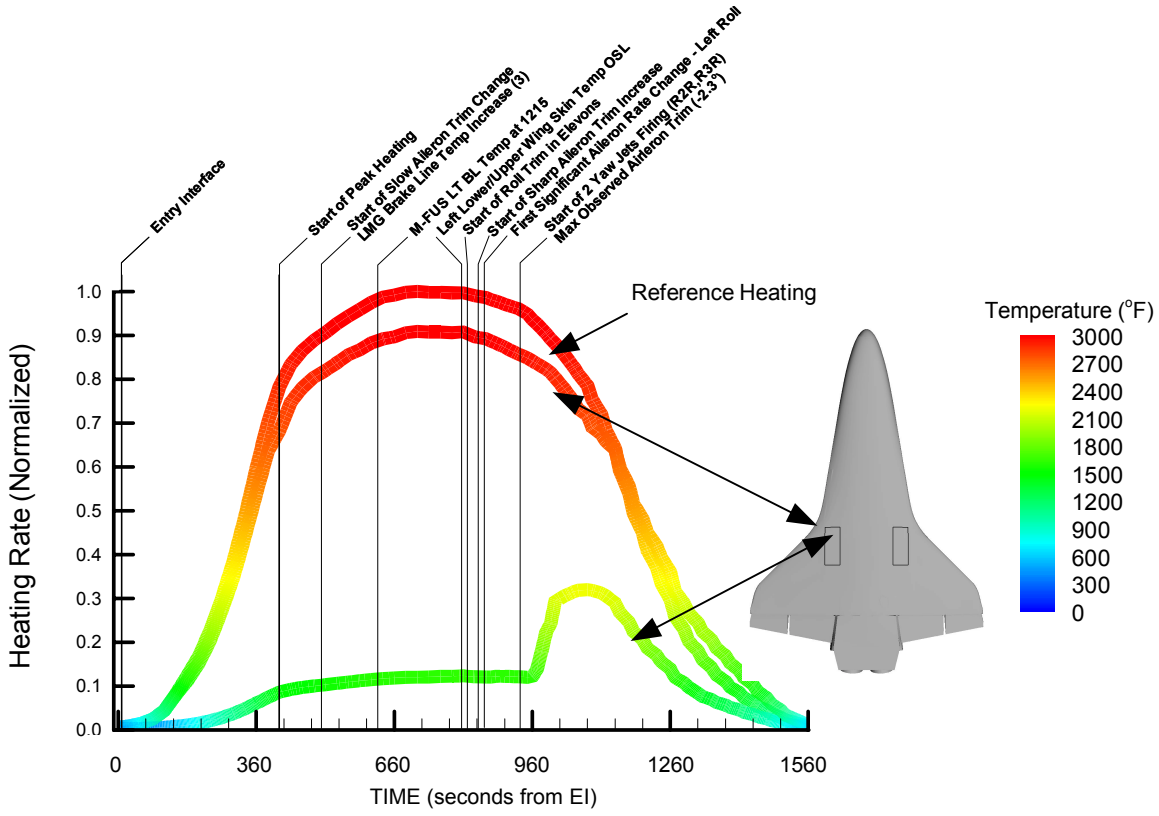

Figure 5-28. STS-107 entry heating rate profile

The precise timing of the wing spar breach is difficult to determine, and three different techniques were used in an attempt to bound the breach time. These techniques included a structural assessment using the wing leading edge spar measurement, use of a thermal model to predict the time required to burn through the spar insulators and then the honeycomb structure, and a wire failure assessment.

The first technique used the strain response, shown earlier in Figure 5-23. On this plot, the initial strain rise that began at about 8:49:09 EST (EI + 300 sec.) is due to thermal elastic strain. It appears that the spar structural softening occurs at approximately 8:50:09 EST (EI + 360 sec.), followed by loss of the structural integrity, or breach, at

approximately 8:51:14 EST (EI + 425 sec.). This appears to be completed by approximately 8:52:00 EST (EI + 471 sec.). A detailed structural model that attempted to reproduce the thermal strain response observed during this timeframe confirmed this timing. This analysis determined that the location of the spar breach must be within about 15 inches of the spar strain measurement. This would locate the spar breach near the intersection of panel 8/9, as shown in Figure 5-29. The flow through the RCC breach maintained some directionality although it was influenced by the shape of the hole, remaining RCC structure, attach hardware, and leading edge insulators. Overall, this strain response is consistent with an RCC breach in the lower part of panel 8 as previously discussed in Section 5.3. Although it is difficult to pinpoint a precise location of the RCC breach, this analysis supports the argument that the breach was closer to the panel 8/9 intersection and Tee seal 8.

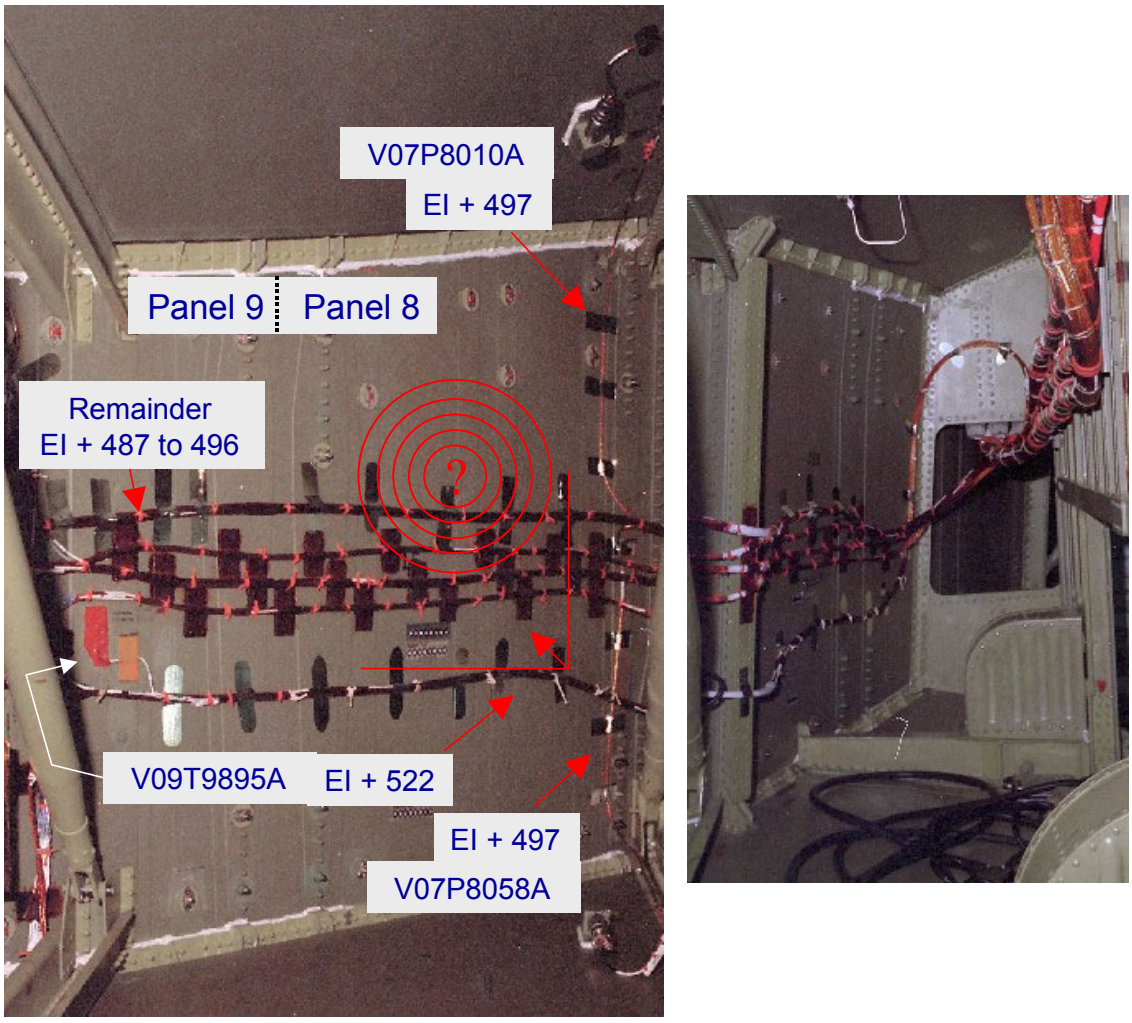

Figure 5-29. Cable routing on wing leading edge and wheel well wall

The second technique used a detailed thermal model to determine the time required to burn through the various insulations immediately in front of the wing leading edge spar (Inconel, Nextel, Cerachrome) and then the honeycomb spar. This model assumed the equivalent heating of a six-inch diameter hole in the bottom of RCC panel 8. Using the expected aero heating rate and the various material properties, the spar burn through occurred at 8:52:19 EST (EI + 490 sec.). This time would be accelerated slightly for a larger diameter hole. The results of this thermal model are shown in Figure 5-30.

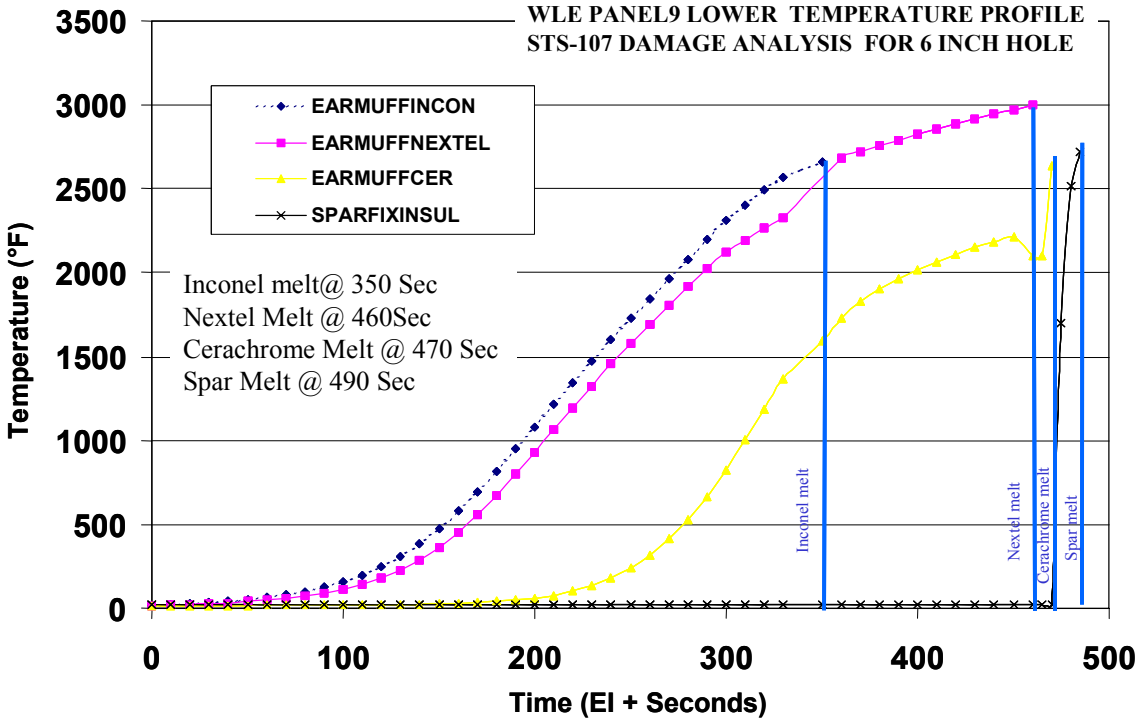

Figure 5-30. Thermal model prediction of wing spar burn through

The final technique used was an examination of the wire failures on the wing leading edge spar. These wire runs are shown in Figure 5-29. The first measurement loss was a MADS upper left wing pressure measurement, which failed at approximately 8:52:16 EST (EI + 487 sec.). This measurement is contained in the upper wire bundle in the left photo in Figure 5-29. The combination of these three separate and distinct analyses results in a range of wing spar breach times as early as 8:51:14 EST and as late at 8:52:16 EST (EI + 425 to 487 sec.).

Immediately after the breach, hot gas inside the wing began to heat the remaining wire bundles that contained real-time telemetry and the recorded MADS measurements. Figure 5-29 shows an inside-the-wing view of the approximate breach location based on this wire failure analysis. The view on the left is of the panel 8/9 spar location. This area is not visible in the right photo, which contains the transition spar and a view of the three wire bundles along the outside of the wheel well wall. Figure 5-31 shows the overall spar breach location with respect to the rest of the wheel well. The distance from the spar to the wheel well wall in this area is approximately 56 inches, as shown in Figure 5-32. Figure 5-33 shows a sketch of the venting of the left wing into the payload bay, driving the direction of the internal flow depicted in Figure 5-31. Note the 142 square inch vent into the midbody fuselage located forward of the wheel well.

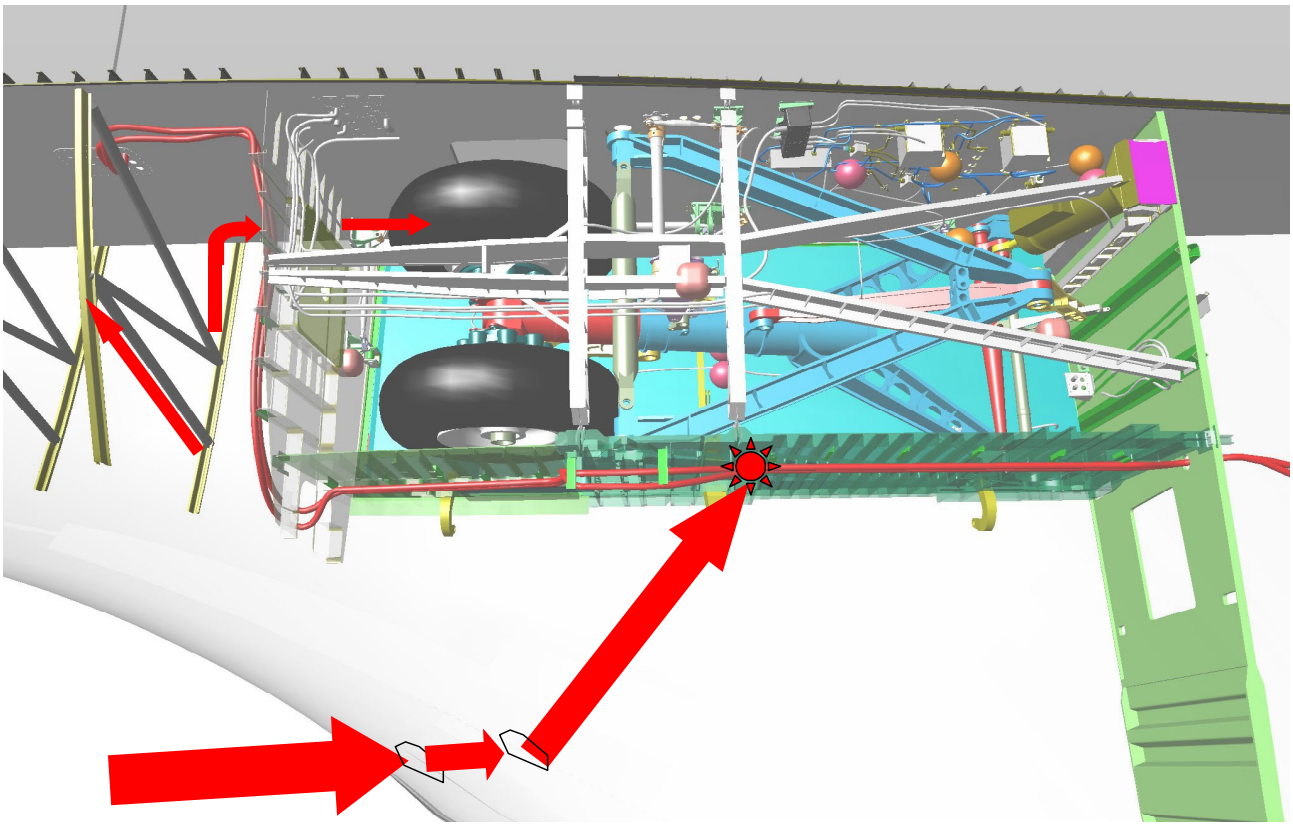

Figure 5-31. Hot gas begins to fill left wing

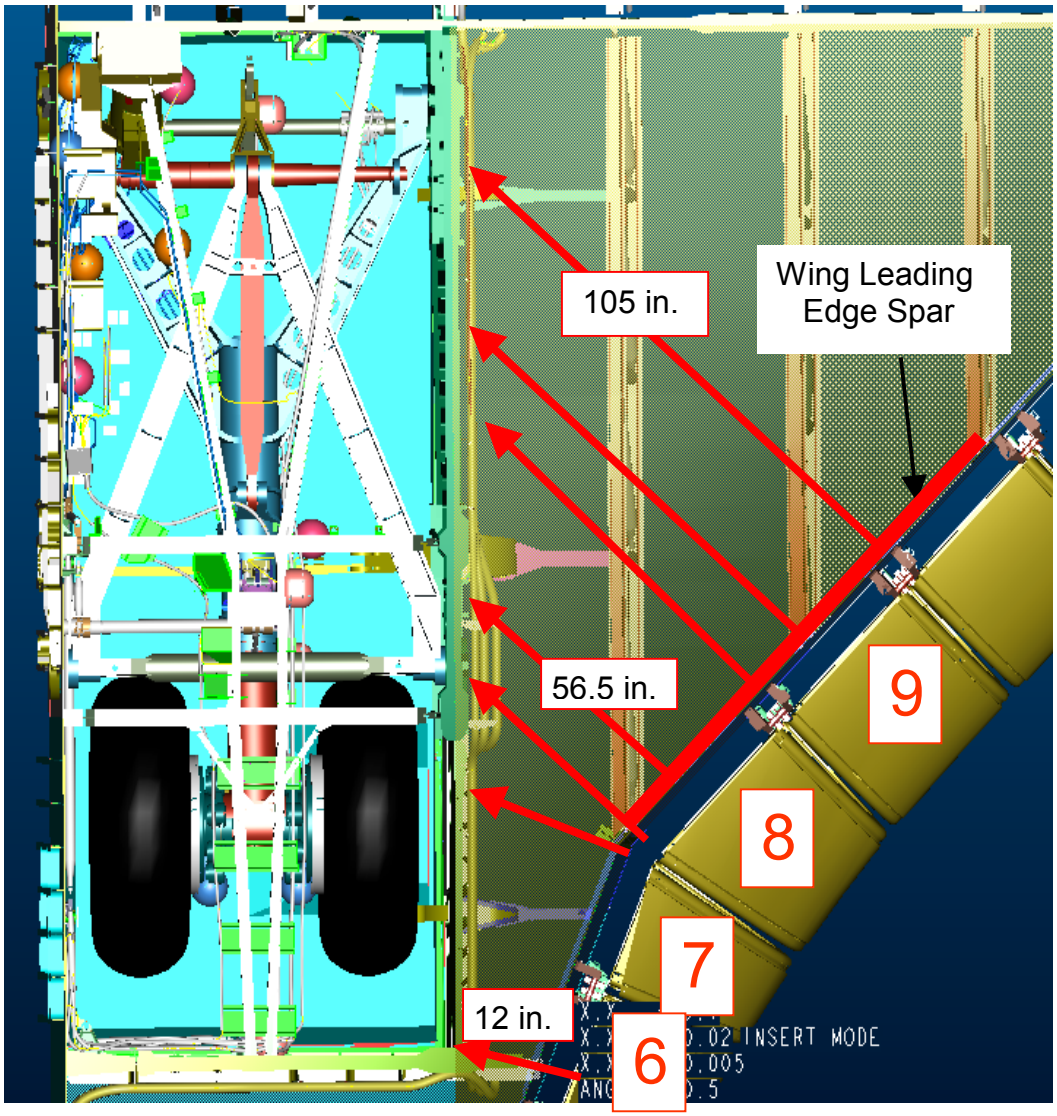

Figure 5-32. Columbia LH wing and wheel well geometry

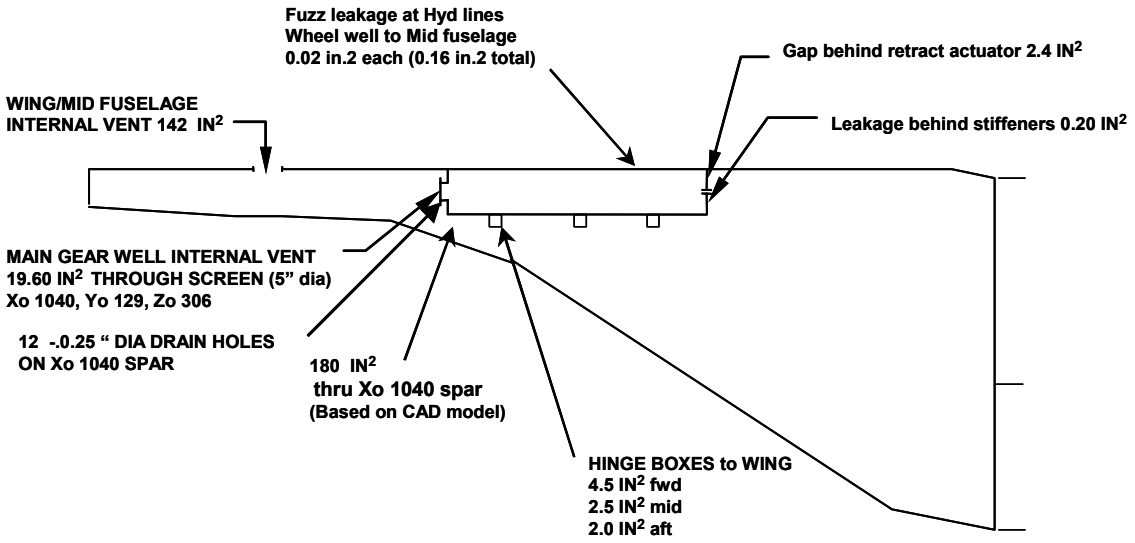

Figure 5-33. Columbia LH wing and wheel well vent model (wheel well leak paths based on Atlantis test comparison)

One hundred sixty-three other measurements failed very quickly over the next two minutes. Figure 5-34 is a plot of the percentage of measurements lost as a function of time from EI. The first measurements to fail are all located on the wing leading edge spar as shown by the purple line on the plot. Bundles 1, 3, and 4 along the wheel well (shown in Figure 5-35) began to fail about 14 seconds after the first spar measurements. This is indicative of a plume impinging on the wire bundles on the wheel well wall.

Arc-jet testing was performed in a facility at JSC to demonstrate how quickly a hole in a 0.1 inch thick aluminum plate would grow in an attempt to determine the feasibility of a rapid spar burn through followed by rapid wire measurement failures. The test configuration had an initial 1-inch diameter hole, and a stagnation heat rate of 12.13 BTU per square foot per second (equivalent to the flight environment at about 8:50 EST, EI ~ 351 sec). During the test, the aluminum plate hole grew from 1 inch in diameter to 5 inches in diameter in approximately 13 seconds. This was consistent with thermal math models developed to analytically predict hole growth. A wire bundle placed 15 inches from the heat source showed very rapid erosion after the hole grew to 5 inches in diameter. The measurement losses in this bundle were very consistent with those observed for wire bundle number 3 (see Figure 5-34). The hole would have grown to a larger diameter; however, the test set-up provided a heat sink that eliminated further hole growth. Overall, the test indicated that a hole in the aluminum honeycomb would grow rapidly, allowing a substantial plume to destroy the wire bundles on the wheel well wall.

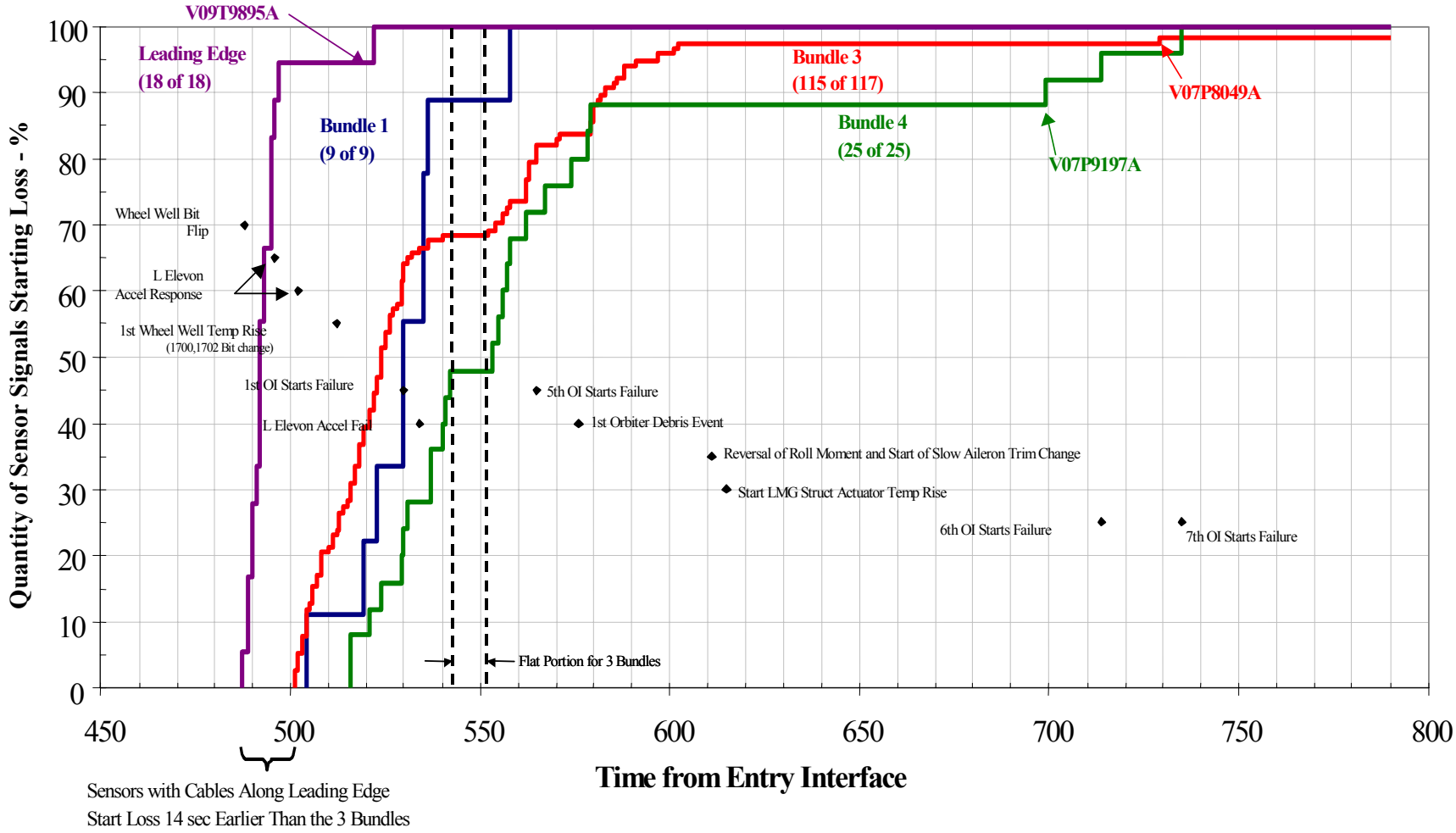

Figure 5-34. MADS data failure due to wire burning

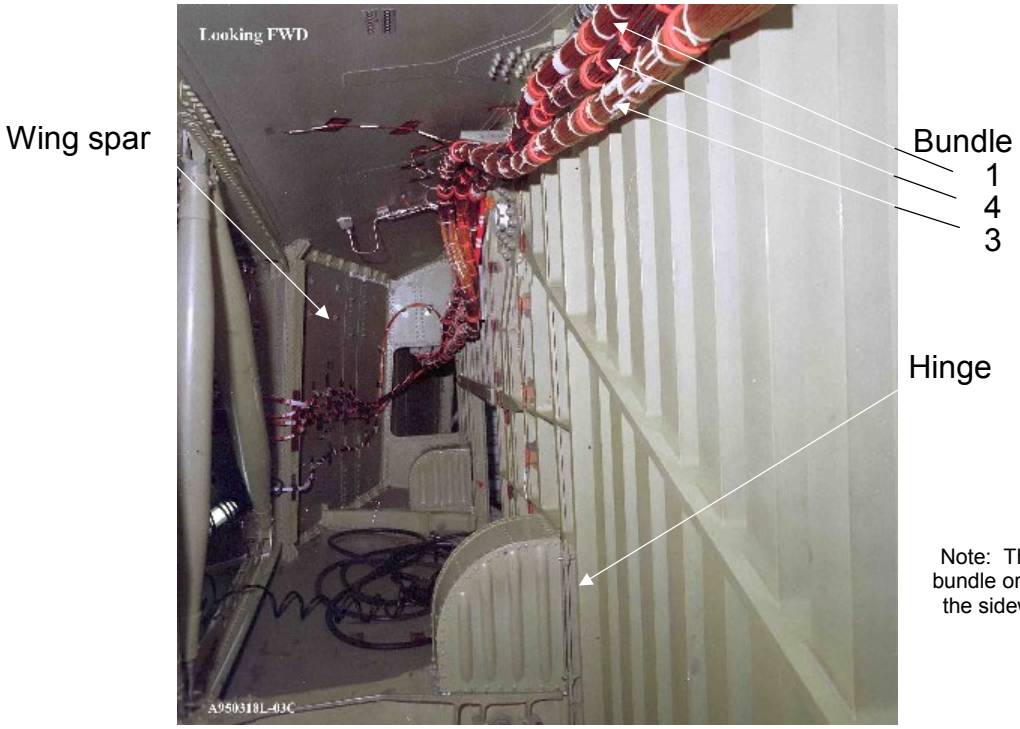

Figure 5-35. View of cables running along outside of wheel wall cavity bulkhead

Four additional measurements failed after 8:54:16 EST (EI + 605 sec.) with the last starting to fail at 8:56:24 EST (EI + 735 sec.). This last measurement failure took over a minute to fail completely. Figure 5-34 and Figure 5-35 show the measurement loss timing and the wire bundle runs along the wheel well. Although almost all measurements internal to the wing failed, two strain measurements on the 1040 spar (forward of the wheel well) were unaffected and produced data until loss of all MADS data at 9:00:13 EST (EI + 964 sec.). Figure 5-36 shows the location of the sensors on the forward wheel well spar. The fact that these measurements are available until loss of data are important indicators that the RCC breach could not be forward on the panel 6 area since these measurements would have been lost as well (see Figure 5-32). These measurements also record key changes in strain that help indicate some of the changes that the left wing underwent as the remainder of the entry events unfolded.

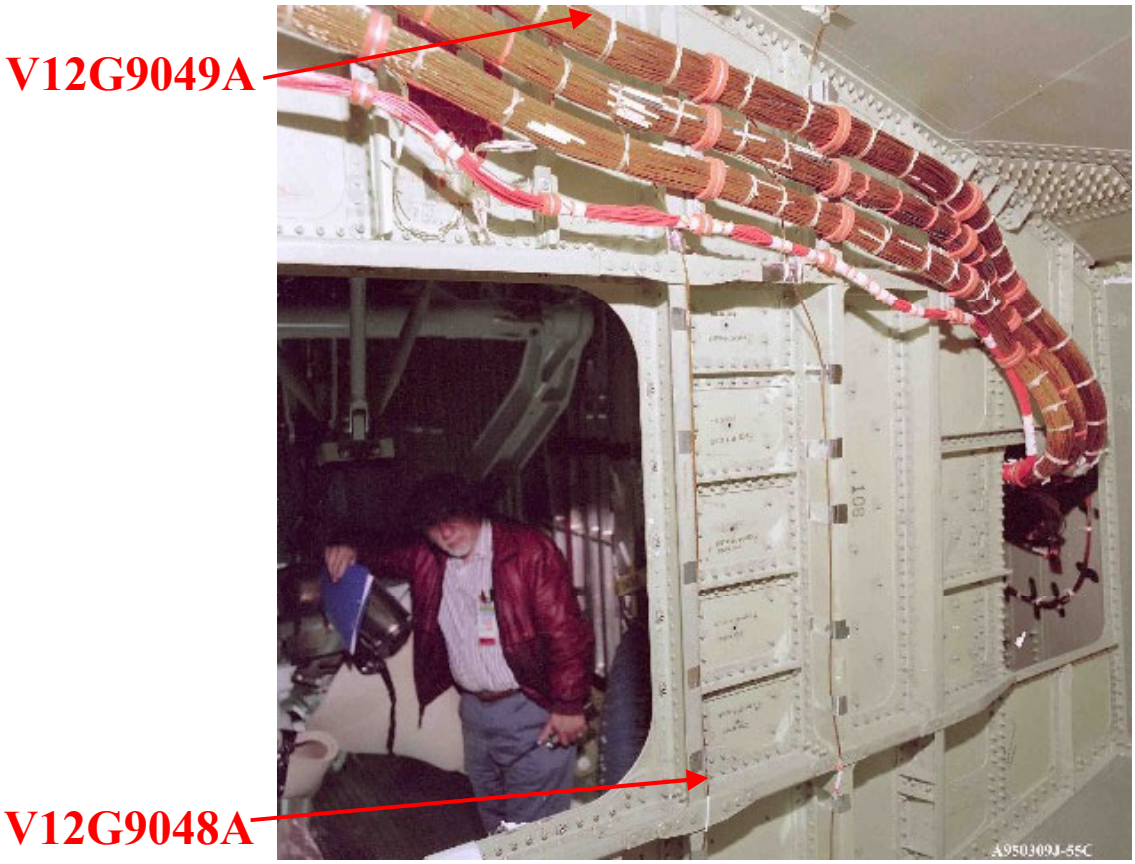

Figure 5-36. Strain measurements on 1040 spar

A comprehensive evaluation of all MADS measurement failures in the left wing was performed to attempt to determine the spar breach progression. Each measurement's failure signature was evaluated to determine both the start time of the failure and when the wire failure was complete. As the wire burns, the short between the twisted pairs of wiring increases thereby producing the time delay effect between failure initiation and complete failure. Eighteen measurements routed on the wing leading edge and over 100 measurements in three wire bundles routed on the outboard side and external to the wheel well were used for this assessment. Seventeen of the 18 wing leading edge measurements failed in 10 seconds starting at 8:52:16 EST (EI + 487 sec.). No other MADS measurements failed during this time. The one measurement that did not fail in this time span was located in the bottom of five harnesses on the WLE. The remaining 17 measurements are in the upper four harnesses with the majority being in the top harness. This would indicate that the spar breach started near the top wire bundle and worked toward the bottom of the spar. Additionally, two of the 18 measurements join the harnesses at the panel 7 to 8 interface, making the wing spar breach outboard of panel 8 very unlikely.

5.4.4 Aerodynamic Events

Coincident with the spar breach at approximately 8:52:09 EST (EI + 480 sec.), the nose cap RCC attach clevis temperature had an off-nominal change in rise rate when compared to previous missions. This rise rate was abnormal for approximately 30 seconds and ended at 8:52:39 EST (EI + 510 sec.). The exact cause of this abnormal temperature rise is not known, but the timing is coincident with the breach of the wing leading edge spar. An explanation is that the abnormal rise is an instrumentation anomaly caused by multiple wire failures in this timeframe. This measurement response is shown in Figure 5-37 along with the same measurement for several other Columbia missions. This figure also shows the location of this internal nose cap measurement on the very forward portion of the left fuselage.

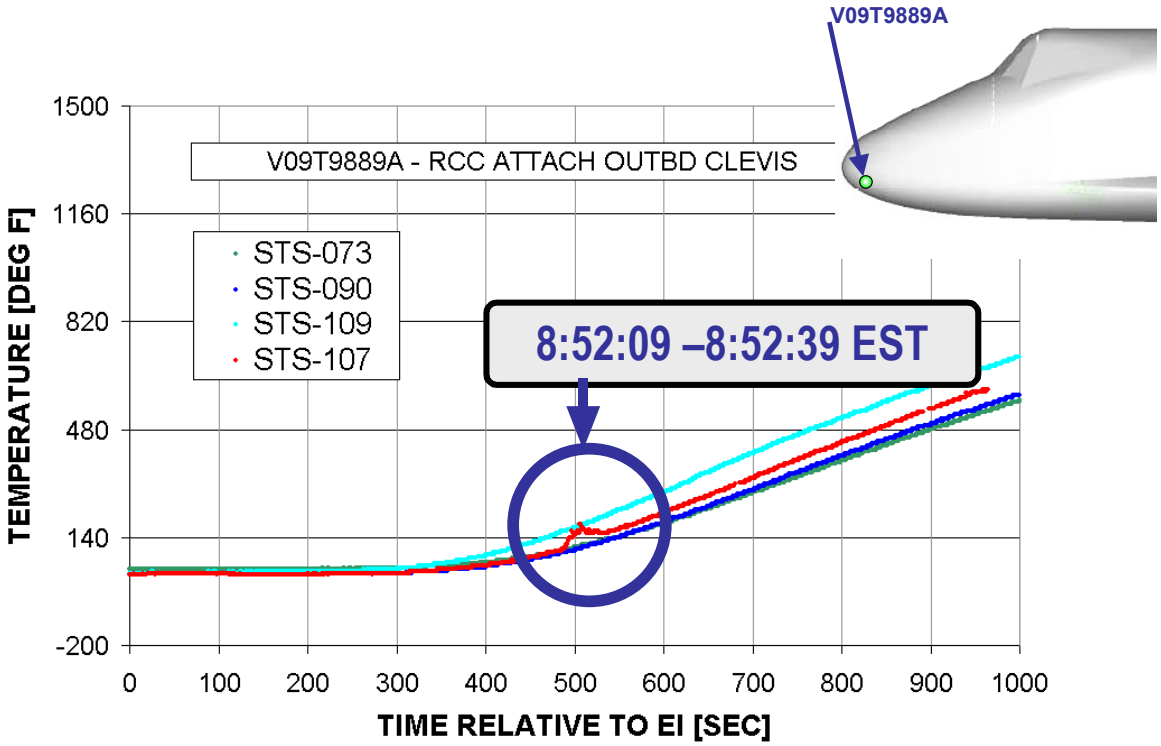

Figure 5-37. Off-nominal temperature rise rate in nose cap RCC attach clevis

Until approximately 8:52:17 EST (EI + 488 sec.), there was no indication of any off-nominal situation that could be observed by the MCC or the crew in real-time. The flight control response and all orbiter telemetry measurements were nominal. The first indication of any anomalous Operational Instrumentation (OI) was a small increase in the left main gear brake line temperature D measurement at this time (see Figure 5-38). Within one second of this time, there is a lower 1040 spar (forward wall of the wheel well) strain measurement that shows an off-nominal increase in strain (see Figure 5-39). These are both indications that the breach in the wing leading edge spar had allowed hot gas to reach the wheel well area, most likely through vent paths around the hinge covers, which allowed hot gas into the wheel well cavity.

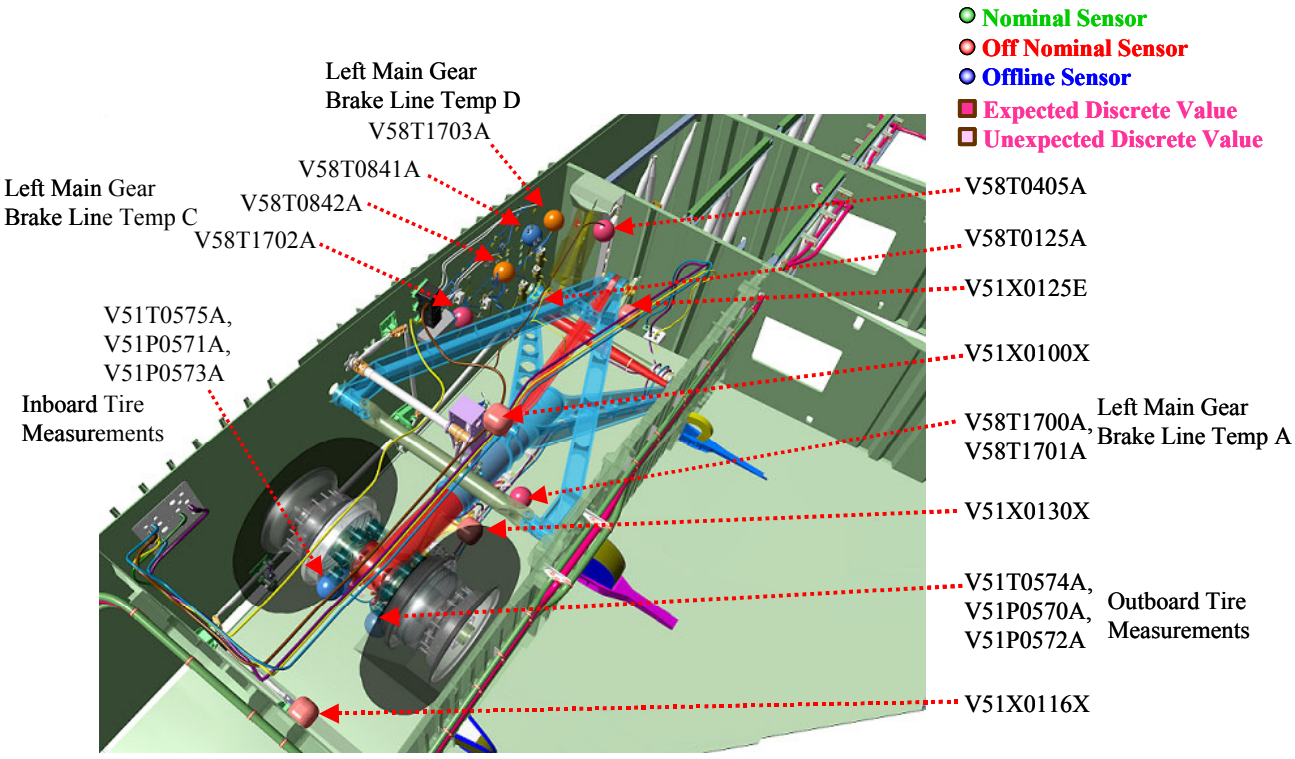

Figure 5-38. Location of sensors in the LH wing wheel well

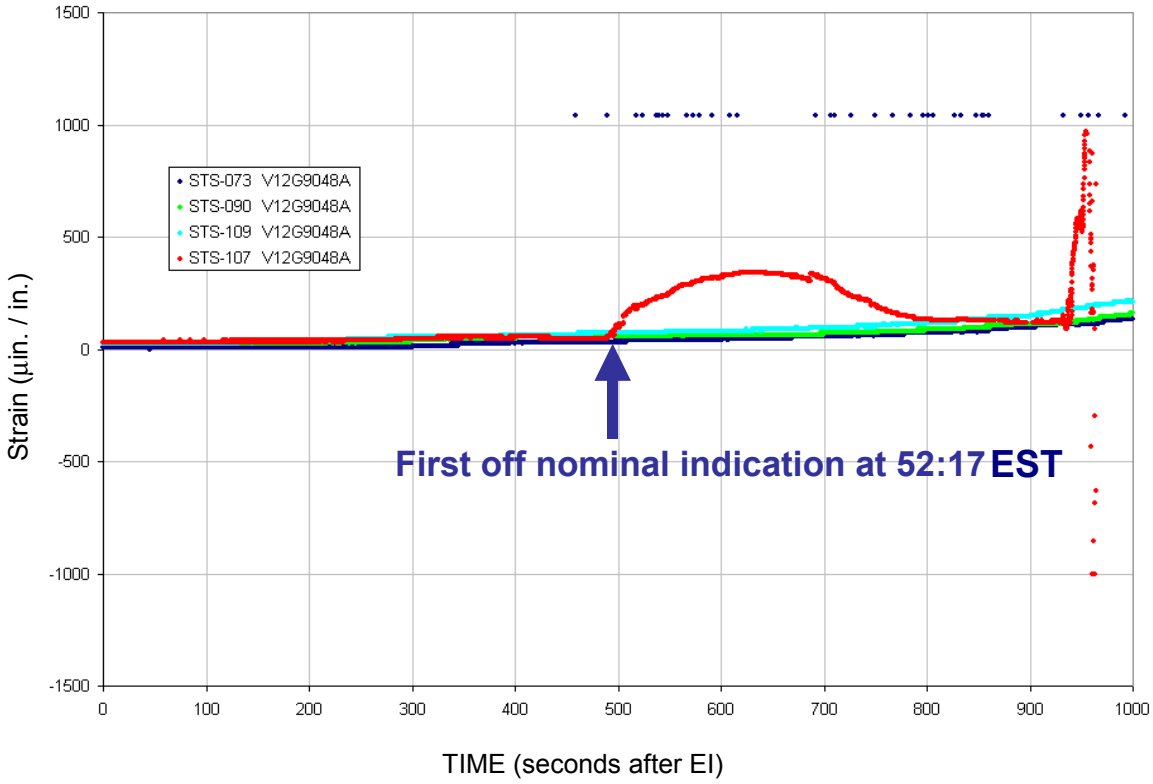

Figure 5-39. Strain rise in lower 1040 spar cap

At approximately 8:52:25 EST (EI + 496 sec.), the left outboard elevon wideband accelerometer showed an unusual 2 g peak-to-peak acceleration (see Figure 5-40). This is consistent with the timing of the many wire failures within the left wing and the timeframe when the spar breach occurs. Additionally, there are two unexplained communication dropouts in this same timeframe. Another 3 g peak-to-peak acceleration anomaly was observed at 8:52:31 EST (EI + 502 sec). Additional temperature measurements (left main gear brake line temp A and C) in the wheel well area (see Figure 5-38) began an off-nominal rise at 8:52:41 EST (EI + 512 sec.).

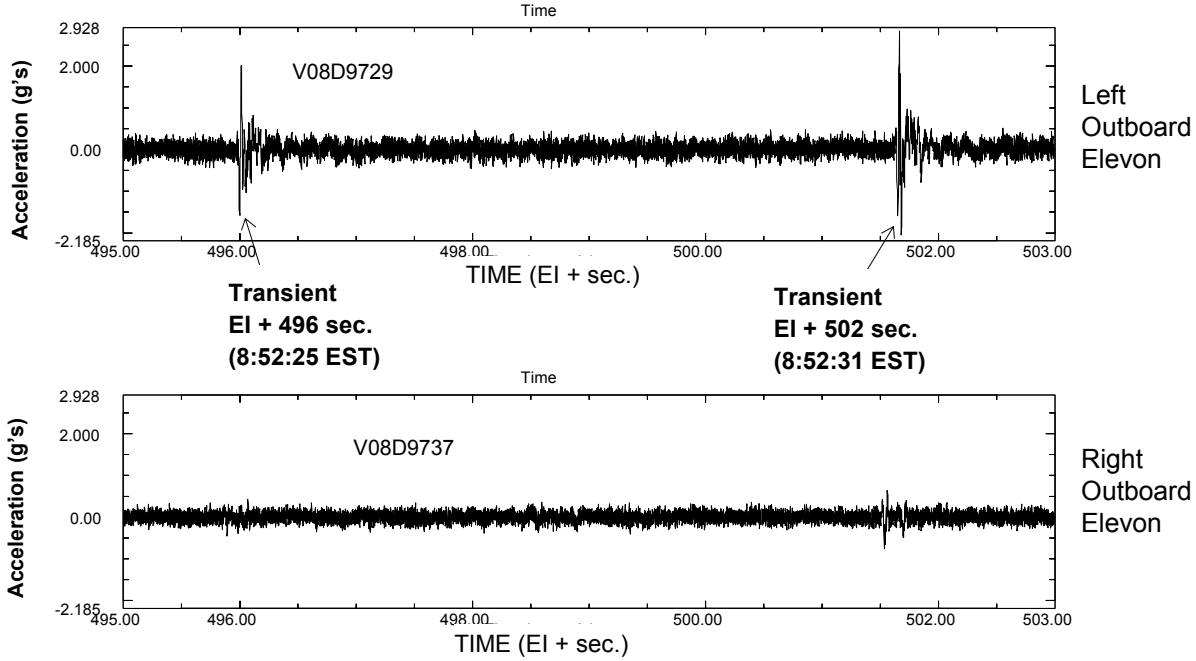

Figure 5-40. Outboard elevon accelerometer responses at 8:52:25 and 8:52:31 EST (EI + 496 and 502 sec.)

The elevon response event was followed by a change in the rise rate for two supply nozzle temperatures and the vacuum vent nozzle temperatures at 8:52:32 EST (EI + 503 sec.). The off-nominal rise rate occurred for approximately 15 seconds for the supply nozzle temperatures and 23 seconds for the vacuum vent temperatures. The location of these nozzles on the left side of the fuselage is shown in Figure 5-41, and the arrow indicates that they could have been located along a line of disturbed flow. The short, abnormal rise rate is unexplained, has not been observed on any previous Shuttle missions, and may not be associated with the upper wing disturbed flow caused by the leading edge damage. Unlike the RCC nose cap clevis temperature, the instrumentation appears to have been valid for both nozzles. Plots of this off-nominal temperature rise for one of the supply nozzle temperatures and the vacuum vent nozzle are shown in Figure 5-42.

Immediately following these events, at 8:52:44 EST (EI + 515 sec.), the aerodynamic roll and yaw coefficients that have been extracted from the flight data showed a slight negative trend (see Figure 5-43). This is indicative of more drag and decreased lift on the left wing.

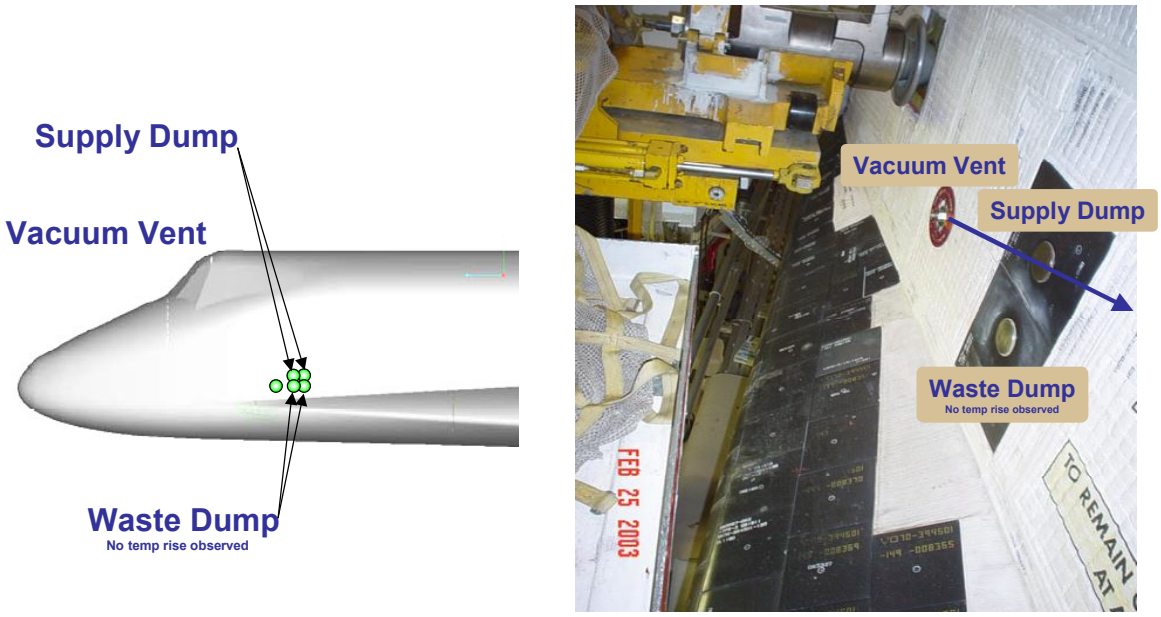

Figure 5-41. Location of supply dump and vacuum vent nozzles

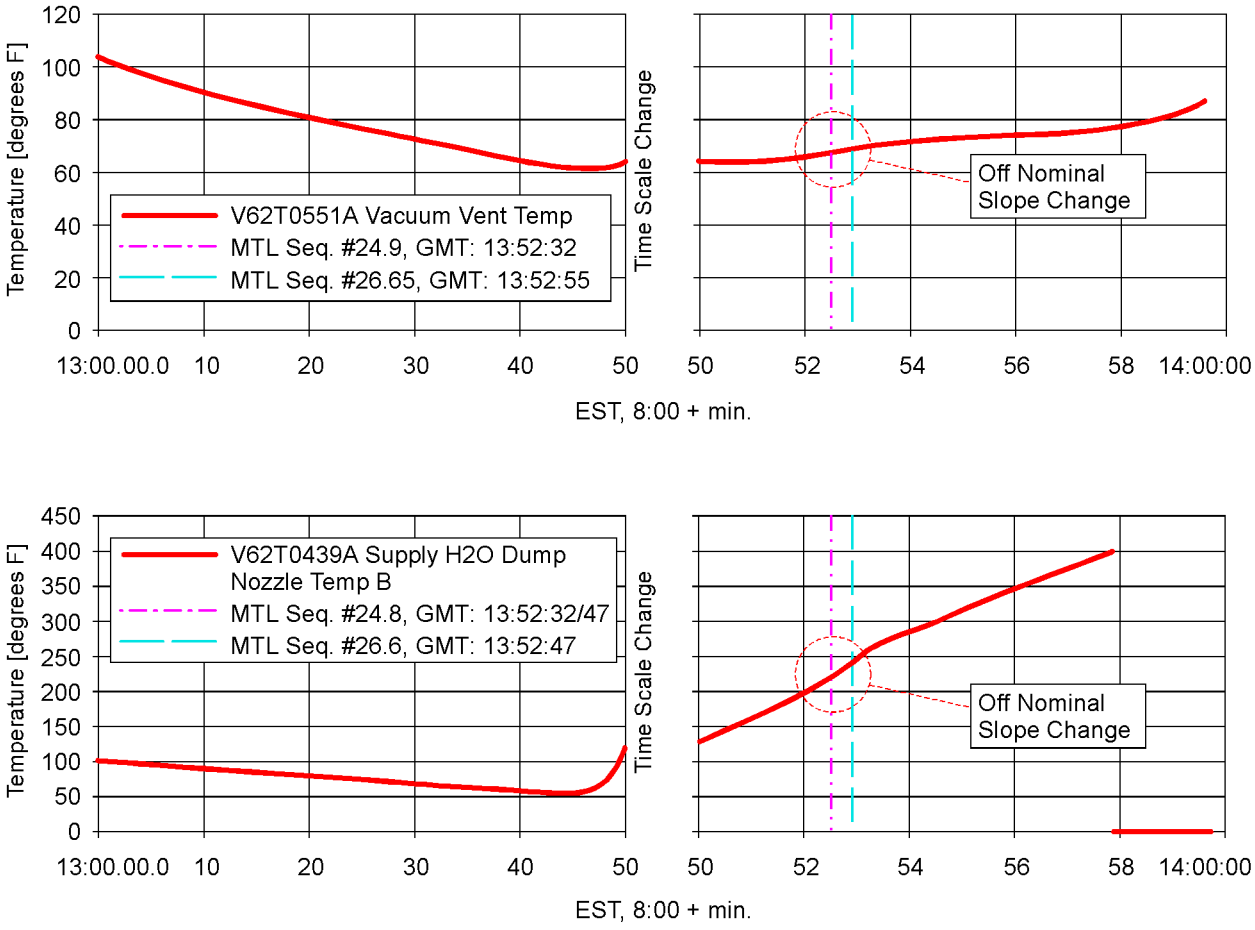

Figure 5-42. Off-nominal temperature for supply nozzle and vacuum vent nozzle

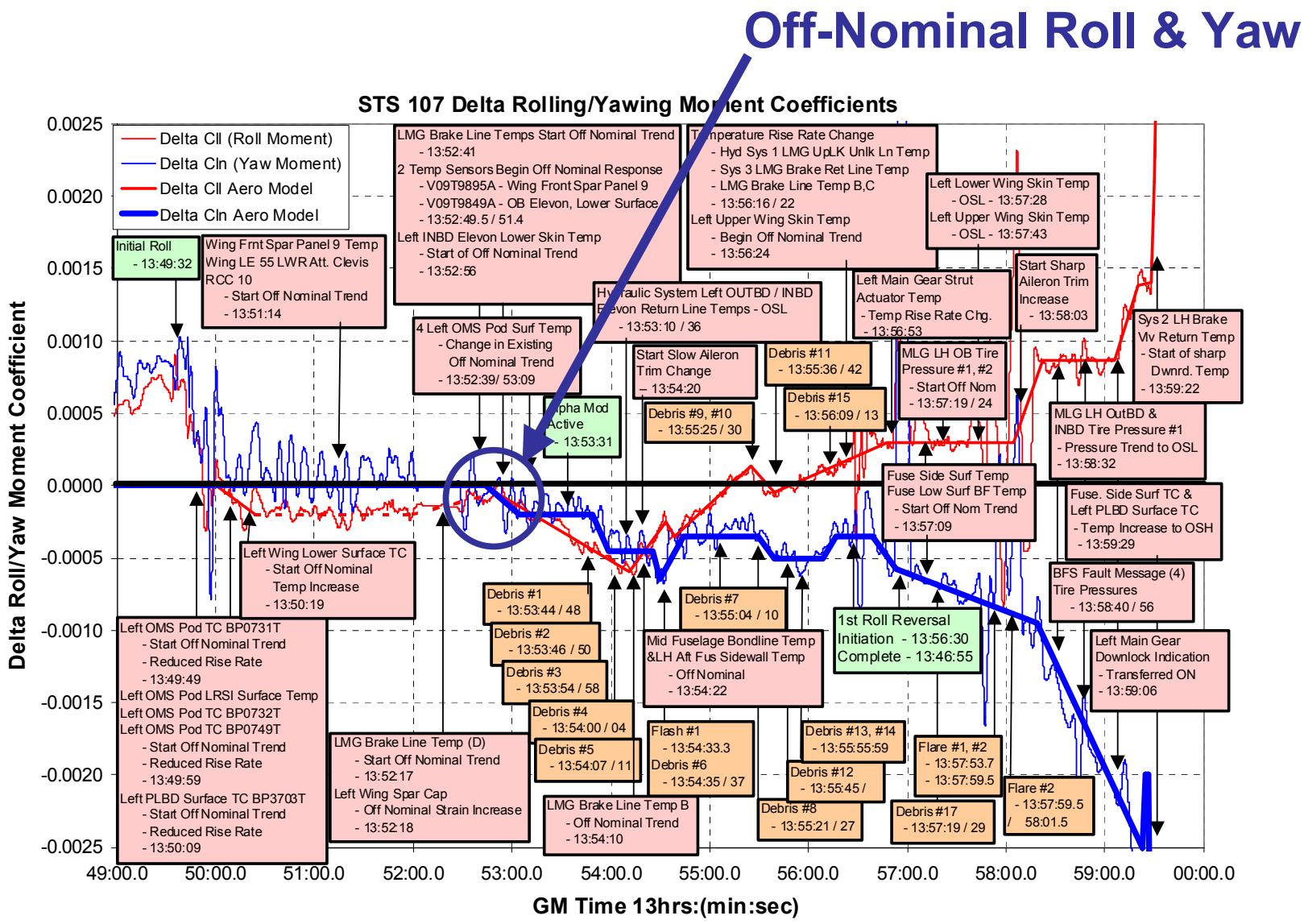

Figure 5-43. First noted off-nominal aero event (Greenwich Mean Time, GMT, is EST + 5 hours)

Hypersonic wind tunnel tests indicate that both the slight negative roll and yaw deltas can be explained by leading edge damage in the lower half of RCC panel 8. This will be discussed in more detail in Section 5.4.5.

The flight control system compensated for the initial aerodynamic disturbance, and the aileron trim continued to match pre-entry predictions. To account for the increased drag the orbiter yawed slightly to the right to balance the yaw moments. The inertial sideslip exceeds flight history at 8:53:38 EST (EI + 569 sec.); however, this small departure was well within the vehicle's capability to control. There was also another communication dropout in this timeframe (8:52:49 to 8:52:55 EST, EI + 520 to 526 sec.).

By 8:53:28 EST (EI + 559 sec.), Columbia had crossed the California coast. After this coastal crossing, there are indications of damage progression on the left wing since the temperature response on the upper surface changes and measurement losses continue in the left wing. At 8:53:29 EST (EI + 560 sec.), several left fuselage temperature measurements showed an unusual 400 degree temperature increase over the next minute. These measurement increases were accompanied by another short communications dropout.

At 8:53:39 (EI + 570 sec.), four left OMS temperature measurements also exhibited an unusual temperature rise. This temperature rise is attributed to shifting of the left wing leading edge upper surface vortices due to interaction with disturbed flow caused by damage progression in the RCC panels 8 through 9 area. During this same timeframe, the upper cap strain gauge on the 1040 spar began an off nominal increase indicating continued heating internal to the left wing.

By this point in the entry almost all measurements in the left wing had been lost and there appeared to be a temporary decrease in the measurement failure rate. It is possible that the "lull" in measurement failures was caused by a release of upper wing skin and FRSI. The breach in the upper wing surface and resulting pressure differentials internal to the wing would shift the internal plume impingement location relative to the wiring. In this same timeframe, there were multiple debris events captured on video by public ground observers beginning at 8:53:46 EST (EI + 577 sec., 20 seconds after California coastal crossing) and ending at 8:54:11 EST (EI + 602 sec.). The source of the debris may be upper wing skin and other thermal protection system (TPS) elements.

Since the wing had been ingesting hot gas for over two minutes, it is quite probable that significant internal damage to the wing occurred over this timeframe. The aluminum structure in the wing was not designed for high heating and many of the components are unlikely to survive this heating environment. For example, aluminum's melting point is ~1200 ^{o}F, but the ingested gas into the wing may have been up to 8000 ^{o}F near the breach. There were other communication dropouts in this timeframe as well (8:53:32 to 8:53:34 EST, EI +563 to 565 sec.).

In the 8:54:10 to 8:54:35 EST (EI + 601 to 626 sec.) timeframe, several key events occurred. The first event at 8:54:10 EST (EI + 601 sec.) was an indication that the temperatures in the wheel well had a greater rise rate, indicating the sneak flow or breach into the wheel area had increased. The roll moment trend changed sign at 8:54:11 EST (EI + 602 sec.) almost simultaneously with the change in wheel well temperature rise rate as shown in Figure 5-44, followed by a debris flash event at 8:54:33 EST (EI + 624 sec.). A large debris item, labeled debris event six, was seen leaving the orbiter two seconds later. This debris event and the roll moment trend change are believed to be created by growing damage to Columbia's left lower wing.

There are several theories that attempt to explain this response including a change in the wing camber or shape due to deformation and a lower wing recession, caused by the loss of much of the support structure internal to the wing. Wing recession here is in reference to structural deformation of the wing surface. In this case, one or more areas on the lower wing form a more concave shaped depression of wing skin and tiles as a result of the structural support in those areas being weakened or lost. A structural analysis of both wing deformation due to the loss of three ribs internal to the wing, and the wing recession concept was performed.

Structural and aerodynamic analysis of wing deformation was performed without any type of recession in the wing lower surface. An assumption of 70 pounds per square foot was used for wing loading. Heat transfer coefficients were updated from previous coupled venting and thermal models for the left wing. A structural model was used along with the heating equivalent of a 10 inch diameter breach in the wing spar beginning at 8:52:16 EST (EI + 487 sec.) assuming 100 percent of the energy from this hole was transferred to the wing interior. Two different cases were analyzed: one with no breach in the upper wing skin and another with a 5 inch diameter breach in the upper skin at 8:54:37 EST (EI + 628 sec.) when a significant visual flash event was observed. Both cases showed that the temperatures of the wing skins, wing spars, and the wheel well wall were high enough by 8:58:19 (EI + 850 sec) that significant damage to the wing structure would occur. Figure 5-45 shows the potential area of damage and that significant deformation of the intermediate wing area and/or a recession in the lower surface is possible.

It is difficult to postulate the exact wing deformation that occurred. One case is localized leading edge damage, resulting in global wing deformation. Local deformation was relatively small, less than 1.0 inch in the damage area with a 0.25-inch global increase in wing tip deflection. Delta rolling and yawing moments were calculated for this case, and they were very small, approximately +0.0001 for roll and -0.0001 for yaw. Another case looked at deformation resulting from the loss of three internal ribs. Again, the local deformation was small (approximately 5 inches) and the resulting aerodynamic moments were small. These delta moments are in the correct direction for change in the aerodynamic moments, but are not nearly large enough in magnitude when compared to the flight derived moments for the time after the roll moment trend reversal. To achieve the aerodynamic response observed in the flight data, more significant damage to the wing would have been required.

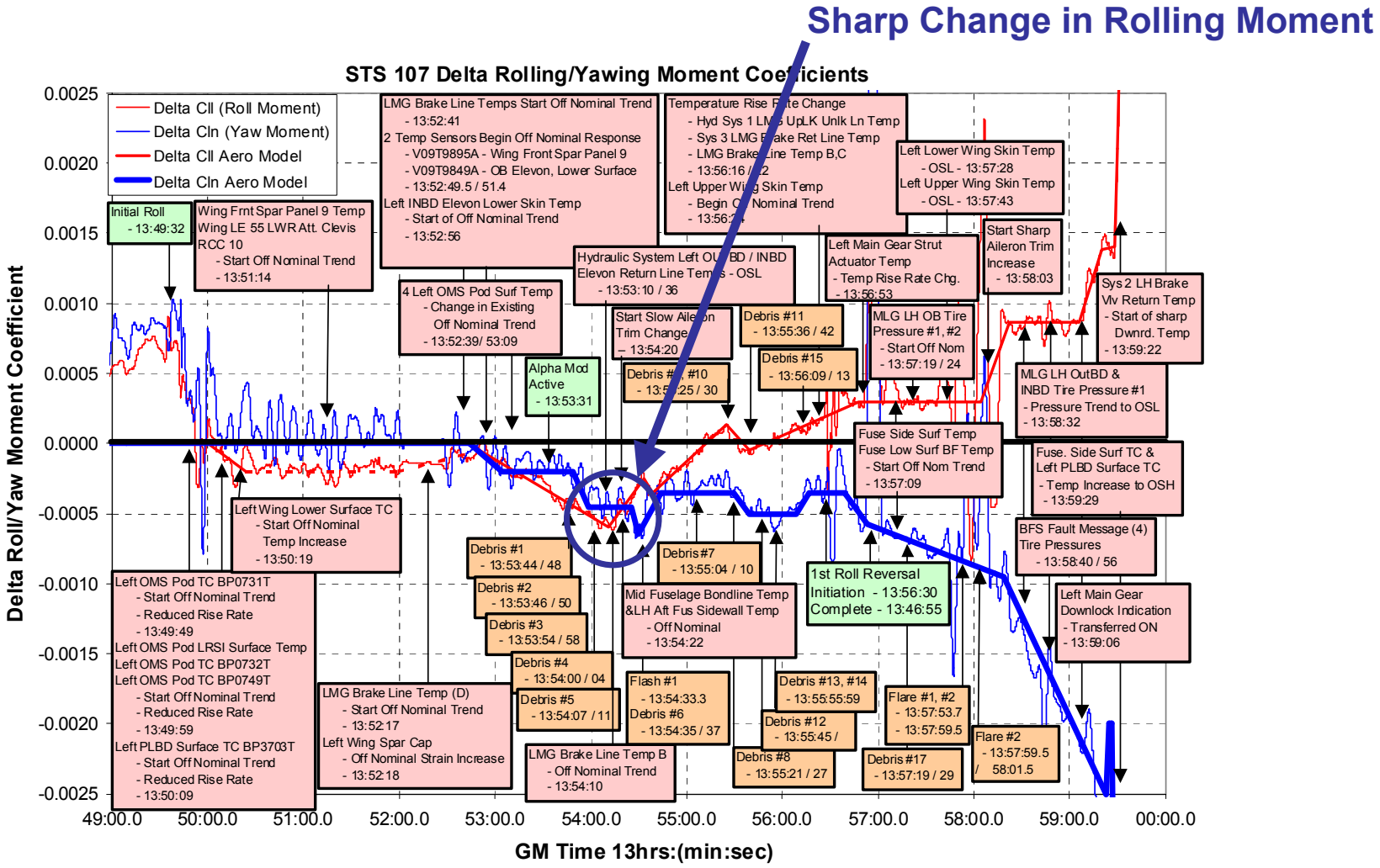

Figure 5-44. Sharp change in rolling moment (GMT is EST + 5 hours)

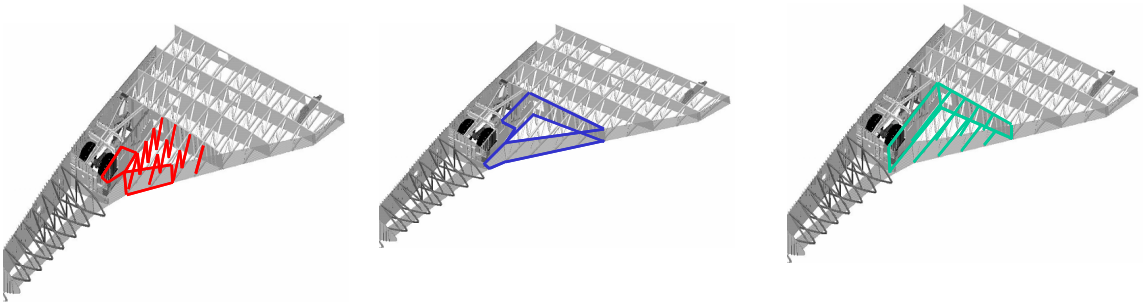

Modulus Reduced to 1%
-Intermediate Rib Struts
-Upper H/C Panels Xo1040 to Xo1140
-WLE Web Aft of RCC Panels 8 & 9

Modulus Reduced by 50%
-Upper & Lower Intermediate
Wing Skin Panels

Modulus Reduced by 30%
-Xo1191 Spar
-Yo167 Rib
-Intermediate Wing Rib Caps

Figure 5-45. Modeling results show potential area of damage and that significant deformation of the intermediate wing area and/or a recession in the lower surface are possible

Based on the structural analysis, it appears feasible that a wing recession occurred and resulted in the large positive slope in the delta rolling moment. The recession was caused by severe prolonged heating internal to the left wing that melted many of the support struts. Once the struts were lost, the wing skin lost structural support, a concave cavity developed, and some lower surface tiles may have been lost. Wind tunnel testing has shown that this type of cavity can cause the change in delta aero moments derived from the aerodynamics reconstruction in this timeframe. The aero moment change is a negative yaw moment due to increased drag and a positive roll moment due to increased lift on the left wing. This testing will be discussed in more detail in the next section.

The flash event in this timeframe could indicate a loss of either upper surface wing skin or thermal blankets or a release of molten material into the environment around the orbiter. More than 10 debris events followed and were observed by various public videos in the 8:55:04 to 8:56:00 EST (EI + 655 to 720 sec.) timeframe. Several of these events were large, consisting of a shower of particles, and lead to a brightening of the plasma trail. Another communication dropout followed at 8:56:00 EST (EI + 720 sec.).

5.4.5 Wheel Well Gas Penetration and Final Aerodynamic Events

By 8:56:16 EST (EI + 727 sec.), hot gas had penetrated the wheel well wall as indicated by off-nominal rates rise rates in several hydraulic line temperatures (see Figure 5-46). Preliminary analysis indicates that it is feasible to have had some gas intrusion into the wheel well area as early as 8:52:39 EST (EI + 510 sec.) since a honeycomb access panel could melt as quickly as 22 seconds after the wing spar is breached. Additionally, there are various vent paths into the wheel well around the landing gear door hinge covers.

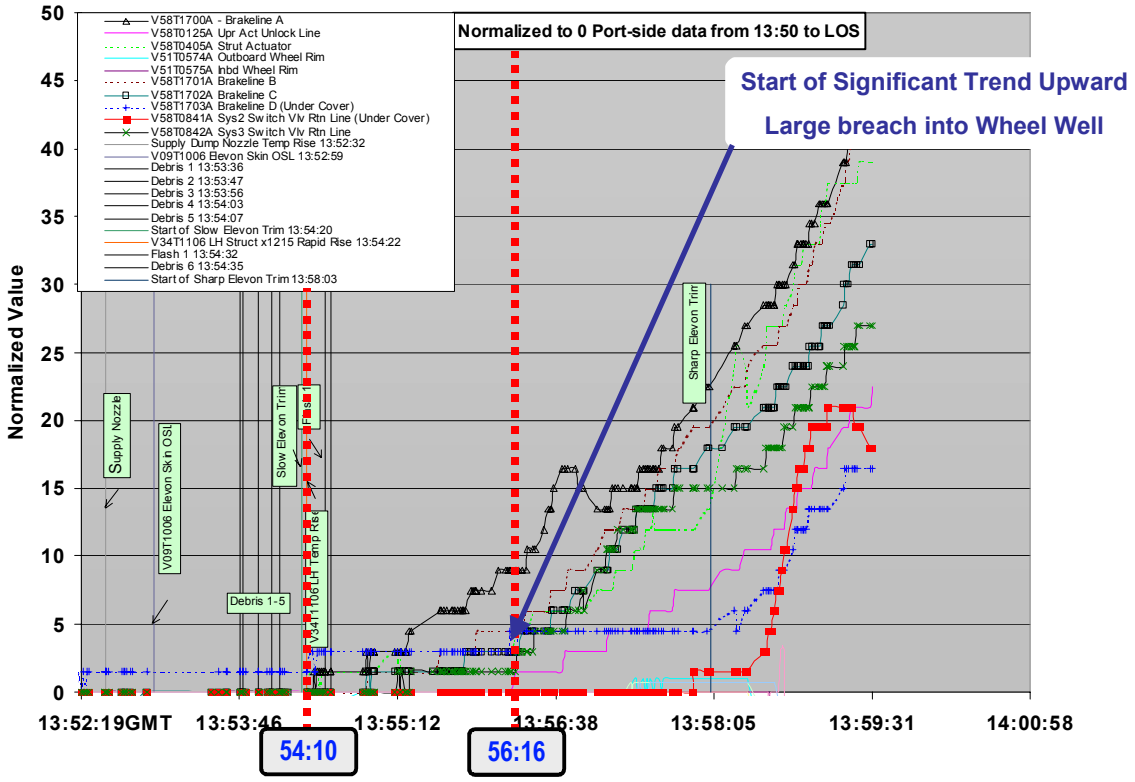

Figure 5-46. Temperature data in left wheel well trends up (GMT is EST + 5 hours)

The centerline of the plume contained enough energy to begin melting the exterior of the wheel well wall by approximately 8:54:00 EST (EI + 594 sec.). The modeling described in the previous sub-section assumed the heating equivalent of a 5 inch diameter hole in the leading edge spar, but does not include the complex thermal interaction with struts and other wing spar structure internal to the wing. The intent of the analysis is to show that it is feasible to obtain the temperature response shown in Figure 5-46, including the early response that was seen in the 8:54:10 to 8:55:10 EST (EI + 601 to 666 sec.) timeframe, when several left main gear brake line temperatures and strut actuator temperatures began an off-nominal rise.

Immediately after the wheel well wall was breached, a hot gas plume began to flow on to the left main gear strut (depicted in Figure 5-47), leading to excessive strut erosion. A wheel well wall breach in this area is consistent with the erosion pattern observed on

the recovered left main gear strut. Even after damage had significantly progressed into the wheel well, the orbiter initiated the first roll reversal at 8:56:30 EST (EI+741 sec.). The maneuver was completed by 8:56:55 EST (EI+766 sec.), and the vehicle was in a normal left bank. The guidance and flight control systems were performing nominally, although the aileron trim continued to slowly change to counteract the additional drag and lift from the left wing.

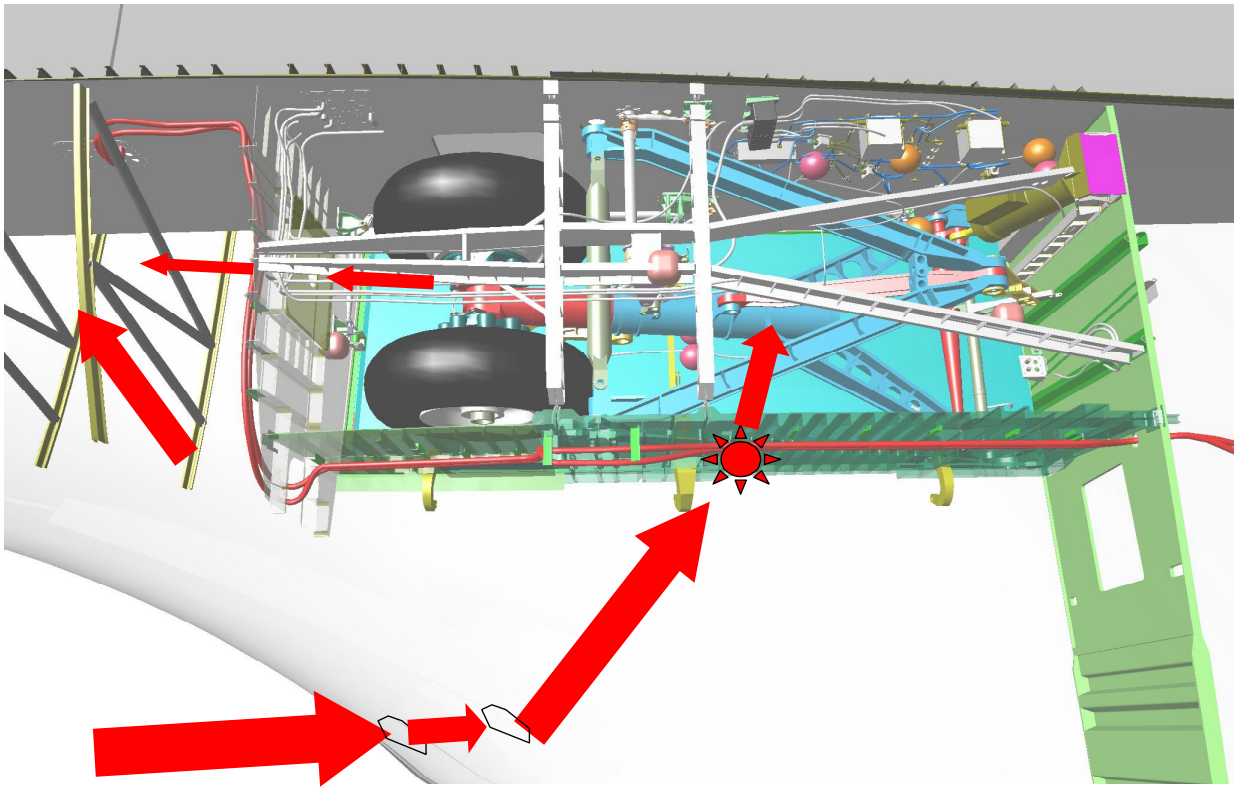

Figure 5-47. Hot gas breaches the wheel well

Imaged at 8:57:14 EST (EI + 785 sec.), the Kirtland photo could indicate a flow disturbance on the leading edge of the left wing and/or flow leaving the leading edge of the left wing (see Figure 5-48). It also appears to show a disturbed flow leaving the trailing edge of the left wing. Other images, not shown here, also show disturbed flow on the upper side of the left wing, indicating that the damage and venting through the upper RCC vent was deflecting the flow upward. The Kirtland photo is a digital still image taken by off-duty employees of the Starfire Optical Range at Kirtland Air Force Base, New Mexico, during the STS-107 entry using a 3.5 inch telescope through a computer controlled 1 meter rotating mirror.

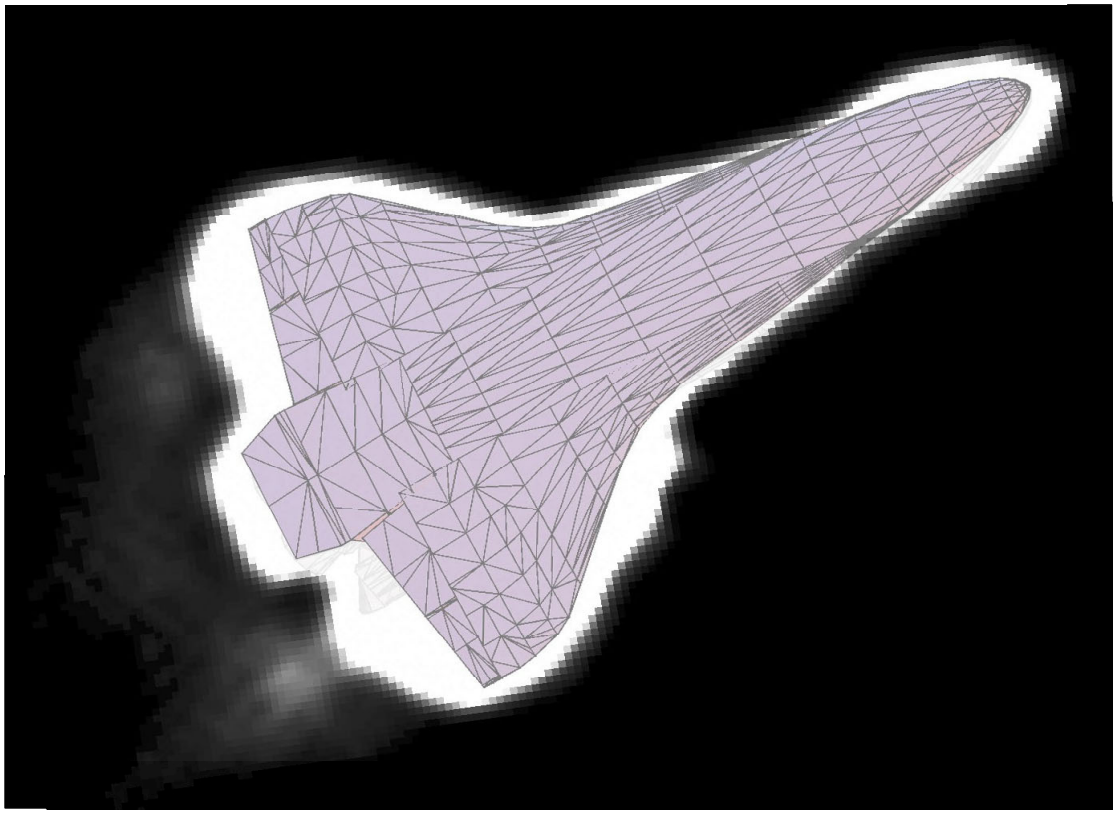

Figure 5-48. Kirtland photo

At 8:58:32 EST (EI + 863 sec.), there was a change in stress measured on the left wing 1040 spar (main landing gear forward wall spar), as indicated by strain gauge measurements that began trending up at 8:52:18 EST (EI + 489 sec.). At 8:58:32 EST (EI + 863 sec.) the lower cap strain (near the bottom of the 1040 spar) essentially returned to a normal measurement when compared to previous flights (see previous Figure 5-39). The upper strain measurement continued to increase during this timeframe indicating that the heating was different on the upper and lower portions of the wheel well and 1040 spar. Although the response of the 1040 spar strain is not completely understood, structural analysis indicates that the strain response can be completely explained by thermal stresses caused by severe heating of the wheel well wall and internal wing components.

As shown in Figure 5-49, this strain response appears to be consistent with another sharp change in the slope of the derived delta rolling moment coefficient that occurred slightly earlier at 8:58:03 EST (EI + 834 sec.), along with several additional debris events. The vehicle responded to this event with a sharp change in the aileron trim. These events indicate that there was another significant change to the left wing configuration at this time. Wing deformation and an increase in the lower surface recession along with a loss of additional bottom tiles are possible explanations for this behavior.

At the same time as the stress was relieved on the lower 1040 spar, two left main gear outboard tire pressures began trending toward an off-scale low reading. This was preceded by a slight upward trend at 8:57:19 EST (EI + 790 sec.) for both pressure measurements. This is an indication of extreme heating of both the left outboard tire and the surrounding instrumentation. The tire has significant thermal mass and substantial heating would be required to produce the slight temperature rise. By 8:58:56 EST (EI + 887 sec.), all left main gear inboard and outboard tire pressure and wheel temperature measurements were lost indicating a rapid progression of damage or wire burning inside of the wheel well. Figure 5-38 shows the location of these pressure sensors.

At 8:59:06 EST (EI + 897 sec.), the left main gear downlocked position indicator changed state. There are indications that the gear did not come down until after Loss of Signal (LOS) because the left main gear uplock position indicator still showed the gear in the stowed position, and the left main landing gear door latch position indicator showed that the door was still closed. Additionally, there are several measurements on the strut that produce valid data until final loss of telemetry in the MCC.

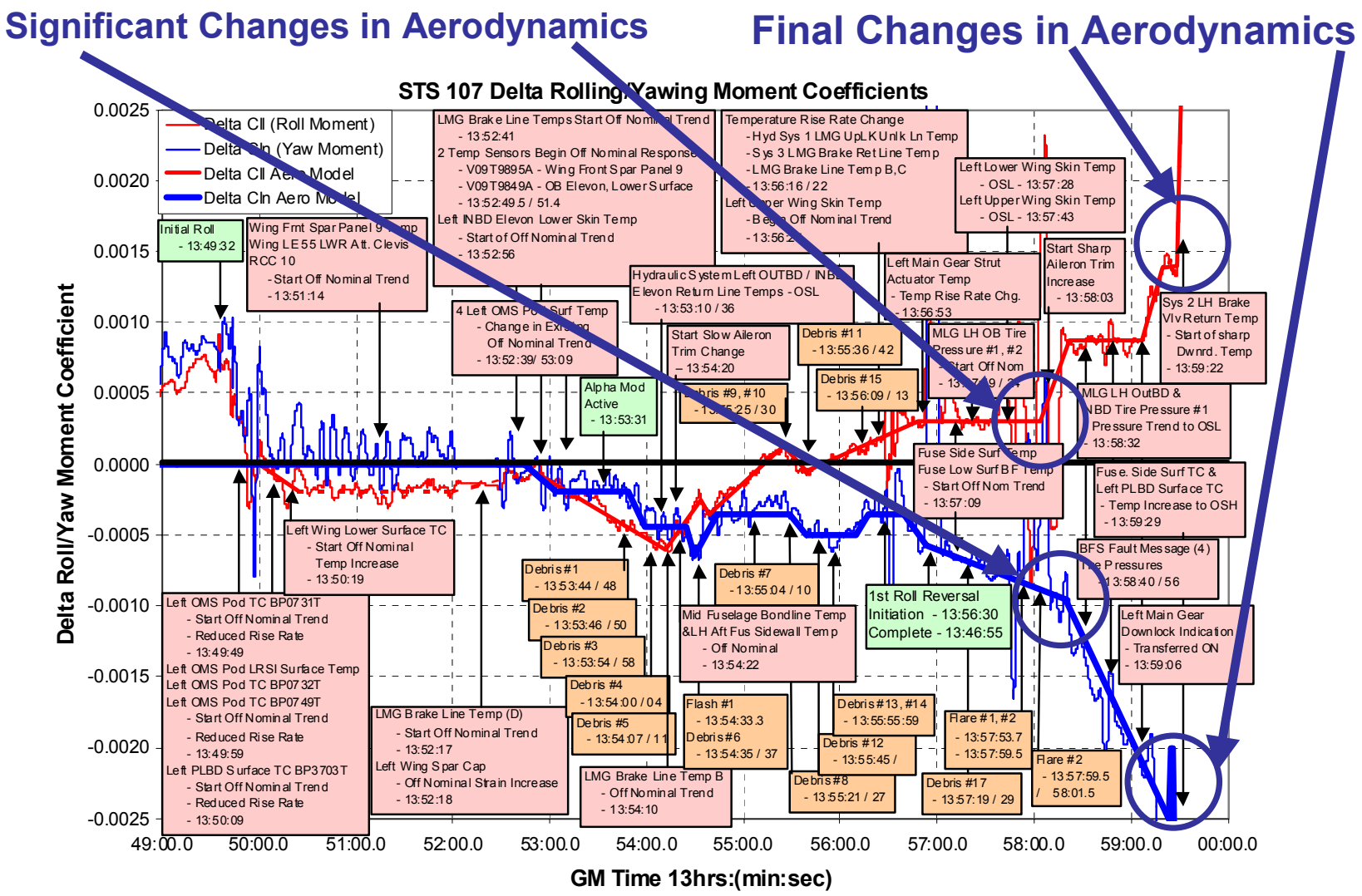

Figure 5-49. Increased wing deformation and wing recession leads to significant vehicle aerodynamic changes (GMT is EST + 5 hours)

As shown in Figure 5-49, there was another abrupt change in the vehicle aerodynamics caused by the continued progression of left wing damage at 8:59:26 EST (EI + 917 sec.). This change was a significant increase in the positive delta roll moment and negative delta yawing moment, indicating increased drag and lift from the left wing. Columbia attempted to compensate for this by firing all four right yaw jets. By this point the MCC had lost all telemetry data at 8:59:23 EST (EI + 914 sec.). Even with all four right yaw jets and a maximum rate of change of the aileron trim, Columbia was unable to control the side-slip angle that was slightly negative (wind on the left side of the fuselage) during much of the entry. The side-slip angle changed sign at 8:59:36 EST (EI + 927 sec.) indicating that vehicle loss of control was imminent (side-slip angle is an aerodynamics terms for the angle between the relative wind velocity and the vehicle direction of motion, or velocity vector).

A large piece of debris was observed leaving the orbiter at approximately 8:59:46 EST (EI + 937 sec.). Five additional debris events and two flash events were observed over the next thirty seconds. MADS recorder data was lost at approximately 9:00:14 EST (EI + 965 sec.) and main vehicle aerodynamic break-up occurred at 9:00:18 EST (EI + 969 sec.), based on video imagery.

In the Mission Control Center, the Entry Flight Control Team waited for tracking data from the Eastern Range and communication link handover to the Merritt Island Launch Area (MILA) ground station. There was no radio frequency (RF) communication received from the vehicle at MILA and no valid tracking data was ever produced at the Eastern Range since the vehicle never crossed the KSC area horizon. Shortly thereafter, Mission Control's Entry Flight Director implemented contingency action procedures.

5.5 AERODYNAMIC RECONSTRUCTION

As previously discussed, the flight-derived aerodynamic moments use the high altitude winds and atmosphere developed by the DAO and represent the most accurate reconstruction that is possible based on available data. Many different scenarios were proposed to define the damage necessary to match this reconstruction using wind tunnel testing and CFD analyses at facilities across the United States. These scenarios include individual and multiple full or partial missing RCC panels, a missing landing gear door, a deployed left main landing gear, missing lower surface tiles, holes through the wing, lower surface deformation, and several others. The details for all of the options that did not match the flight-derived data will not be discussed here and are beyond the scope of this document.

Figure 5-50 through Figure 5-52 show the flight derived delta roll, yaw, and pitch aerodynamic moments, respectively, along with the tested damaged configuration results that are consistent with the flight data. The intent of the remainder of this section is to briefly discuss the CFD analysis and wind tunnel testing used to replicate the derived delta aero moments. Note the time scale on these plots is in seconds from EI.

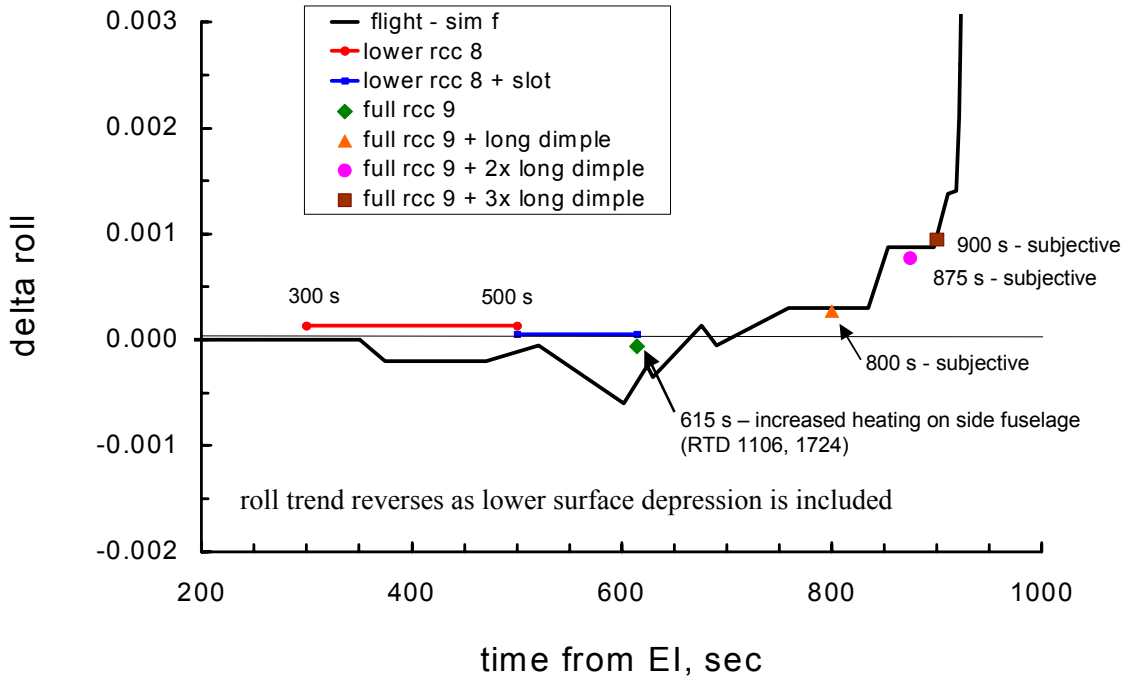

Figure 5-50. Wind tunnel testing configurations that match delta roll moment data

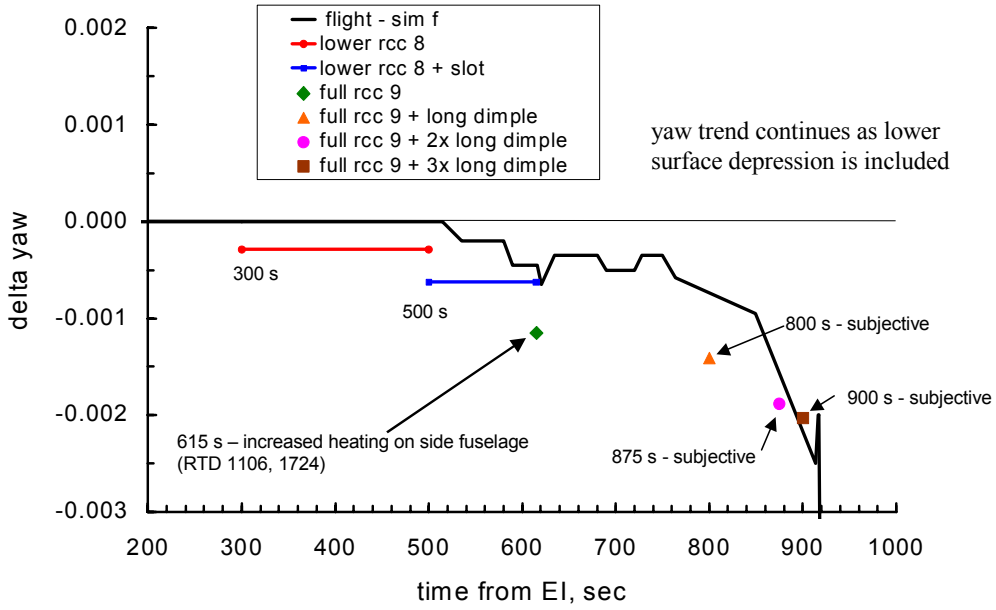

Figure 5-51. Wind tunnel configurations that match delta yaw moment data

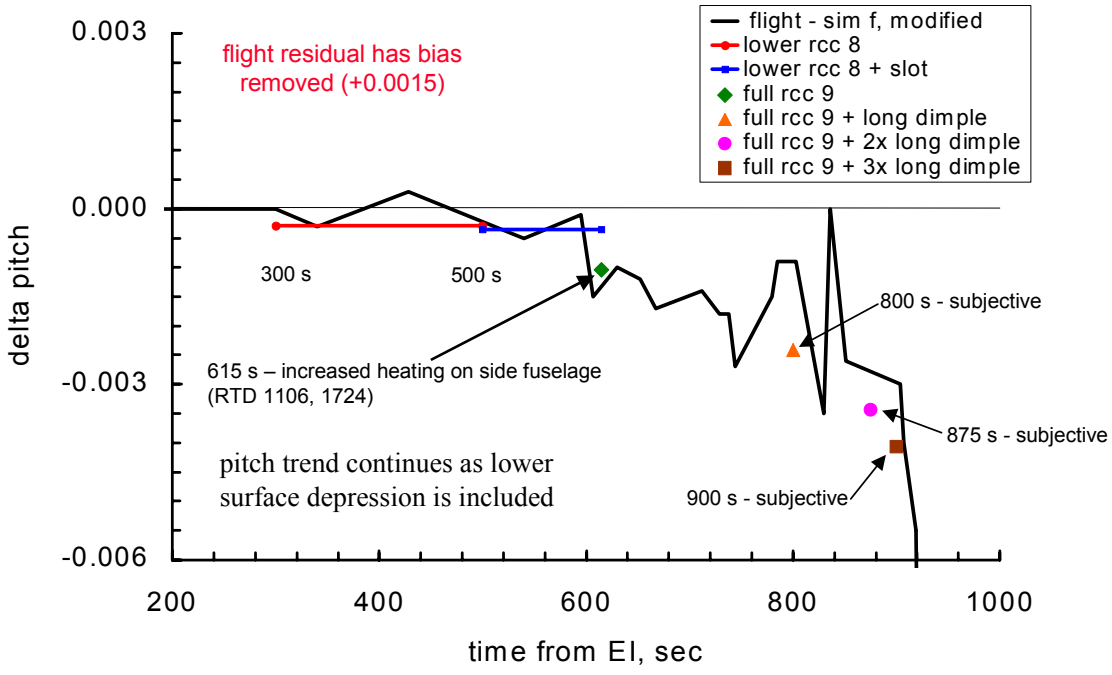

Figure 5-52. Wind tunnel configurations that match delta pitch moment data

As discussed previously, the reconstructed aerodynamic moments showed little to no change due to damage through 8:52:29 EST (EI + 500 sec.). Based on the forensics data discussed in Section 5.3, the most likely region of initial damage was in the lower part of RCC panel 8. Wind tunnel testing in the Langley Research Center (LaRC) CF4 tunnel indicated that a missing bottom part of RCC panel 8 (from the apex to the lower carrier panel) matches the initial aerodynamic increments, which show a minimal effect on the overall vehicle aerodynamics. In fact, even a full missing panel 8 produces only a small change to the roll and yaw aero moments. Figure 5-53 and Figure 5-54 show the results of this LaRC evaluation.

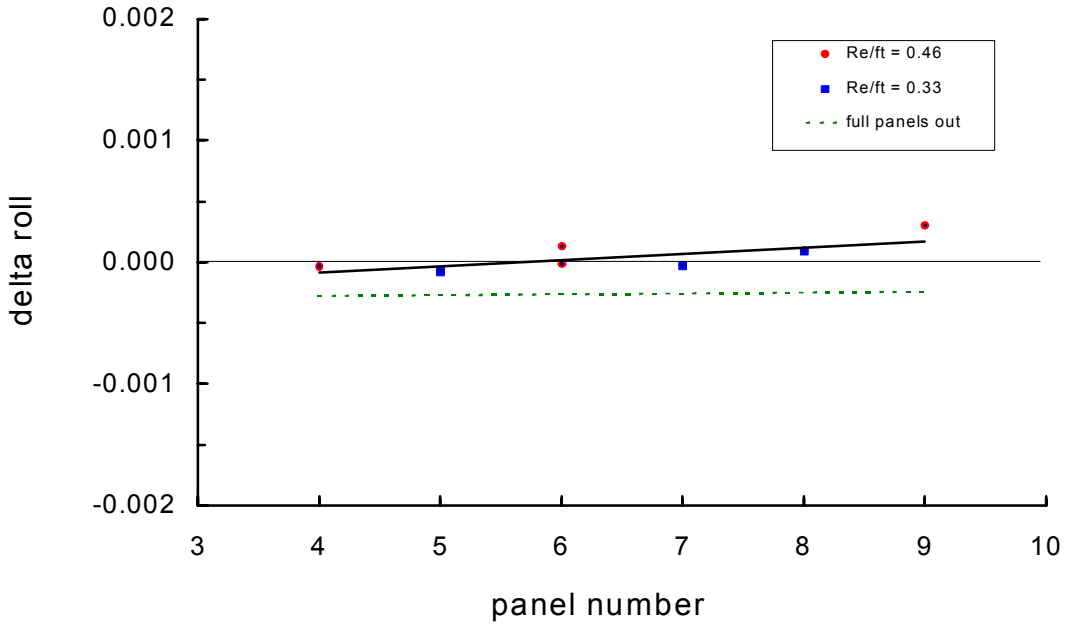

Figure 5-53. Delta roll for lower half and full panel RCC panel missing

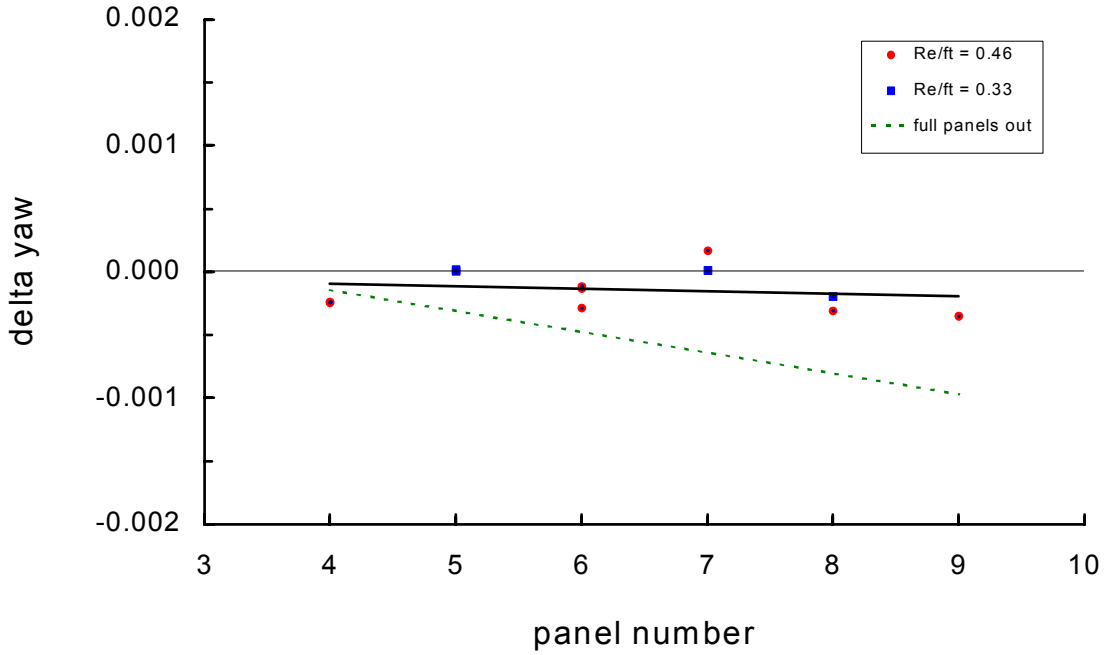

Figure 5-54. Delta yaw for lower half and full panel RCC panel missing

The left wing spar was breached in the 8:51:14 EST (EI + 425 sec.) to 8:52:15 EST (EI + 487 sec.) timeframe. Initially, the spar breach had little to no effect on the derived aero moments. Over time the leading edge damage progressed and a slot or upward deflection of the flow through the upper carrier panel 8 developed. The combination of flow through the wing leading edge and flow through a slot onto the upper carrier panel is consistent with the first observed aerodynamic response, which occurs at 8:52:29 EST (EI + 500 sec.). This can be observed in Figure 5-50 and Figure 5-51 as a slow negative trend in delta roll and yaw. Figure 5-55 shows the wind tunnel test results for three different cases: missing lower RCC panel 8, missing panel 8 combined with a 4 inch diameter hole in the upper carrier panel 8, and missing RCC panel 8 with a slot through the upper carrier panel. The slot was shown to produce the increased delta yaw observed during flight as well as the upper surface flow disturbances on the OMS pod and left side fuselage, which were also observed during flight by abnormal temperature rise rates.

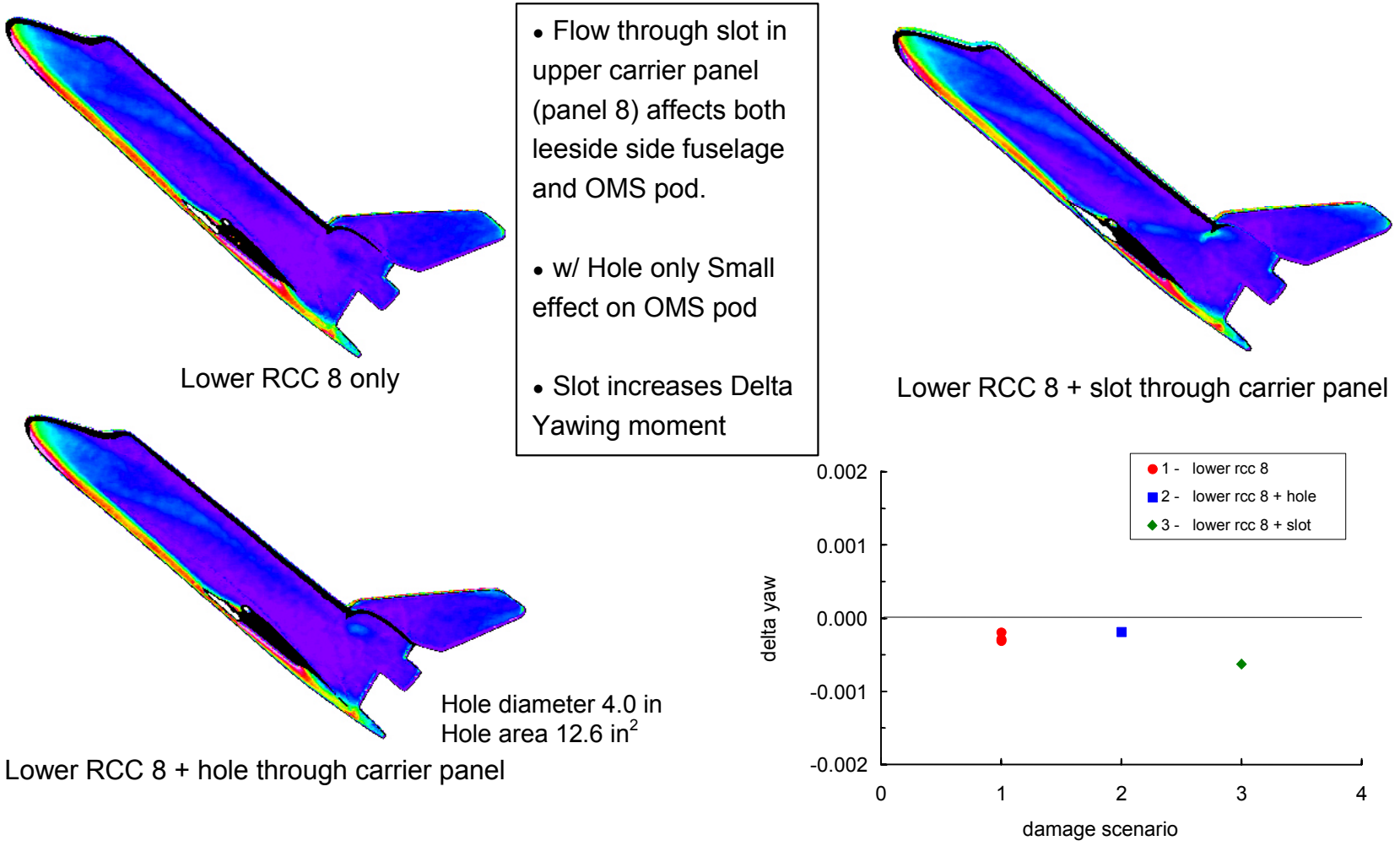

Figure 5-55. Wind tunnel testing results for missing lower carrier panel 8 and a slot and hole through wing

It is possible that a hole through the upper wing developed in the 8:54:11 EST (EI + 600 sec.) to 8:54:31 EST (EI + 630 sec.) timeframe. This is consistent with a lull in the measurement failure rate in the wire bundle along the wheel well that was discussed earlier in Section 5.4.3. Wind tunnel testing and CFD analysis have shown that sizable holes through the wing have little to no effect on the aerodynamics and heating on the left side of the fuselage and OMS pod. A representative sample of this work is shown in Figure 5-55 as damage scenario number 2.

The next significant aerodynamic event occurred at 8:54:11 EST (EI + 602 sec.) when a dramatic reversal of the aero rolling moment trend occurs. By this time hot gas and an internal plume environment had severely degraded the structural integrity of some of the intermediate wing support structure leading to wing deformation. Three different configurations were tested to validate the theory of wing deformation. The first involved global wing deflection of up to 0.79 inches due to damage and is depicted in Figure 5-56. CFD analysis of this configuration showed extremely small aero moment response for yaw and roll that does not match the flight derived data. More substantial local wing skin deformation with a maximum deflection of 5.1 inches due to three ribs missing along with other internal wing damage was examined using CFD tools. Again, these results produced only small aerodynamic moment changes, which did not match the flight-derived data.

- Case 4 Aerodynamic Increments – Global wing deflection due to damage
  Max RMS Delta ΔWing Deflection
  (Nominal – Damaged structure) is 0.79”
  → ΔCl = 0.0001, ΔCn = -0.0001

- Hand Calculation Increments – Local wing deformation due to damage
  Max ΔWing Deflection, Zo = 5.1”
  → ΔCl = 0.000, ΔCn = -0.0001 – Newtonian
  → ΔCl = 0.00005, ΔCn = -0.00014 – Cart3D
  → ΔCl = 0.00012, ΔCn = -0.0001 – FELISA

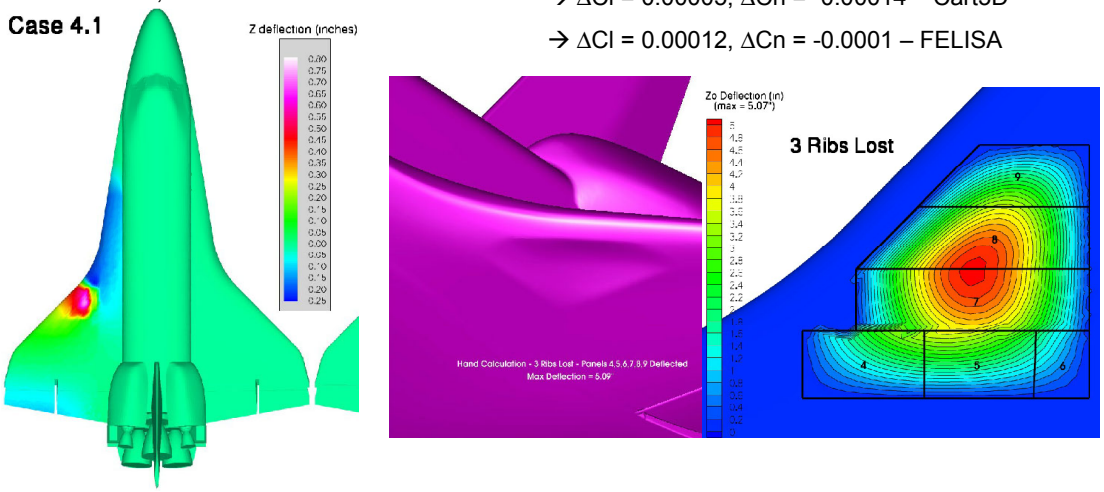

Figure 5-56. CFD analysis of wing deformation

The third and final configuration that was tested was a depression in the lower surface of the wing caused by the significant structural damage caused by the hot gas plume environment internal to the wing. A previous section (5.5.5) discussed the internal

structural damage that was most probable in this timeframe. LaRC wind tunnel testing and CFD analysis were performed for several different configurations of lower surface recessions shown in Figure 5-57. The data shows that it is feasible for a recession to cause the change in the rolling moment sign when combined with some portion of RCC panel 9 missing at 8:54:11 EST (EI + 602 sec.).

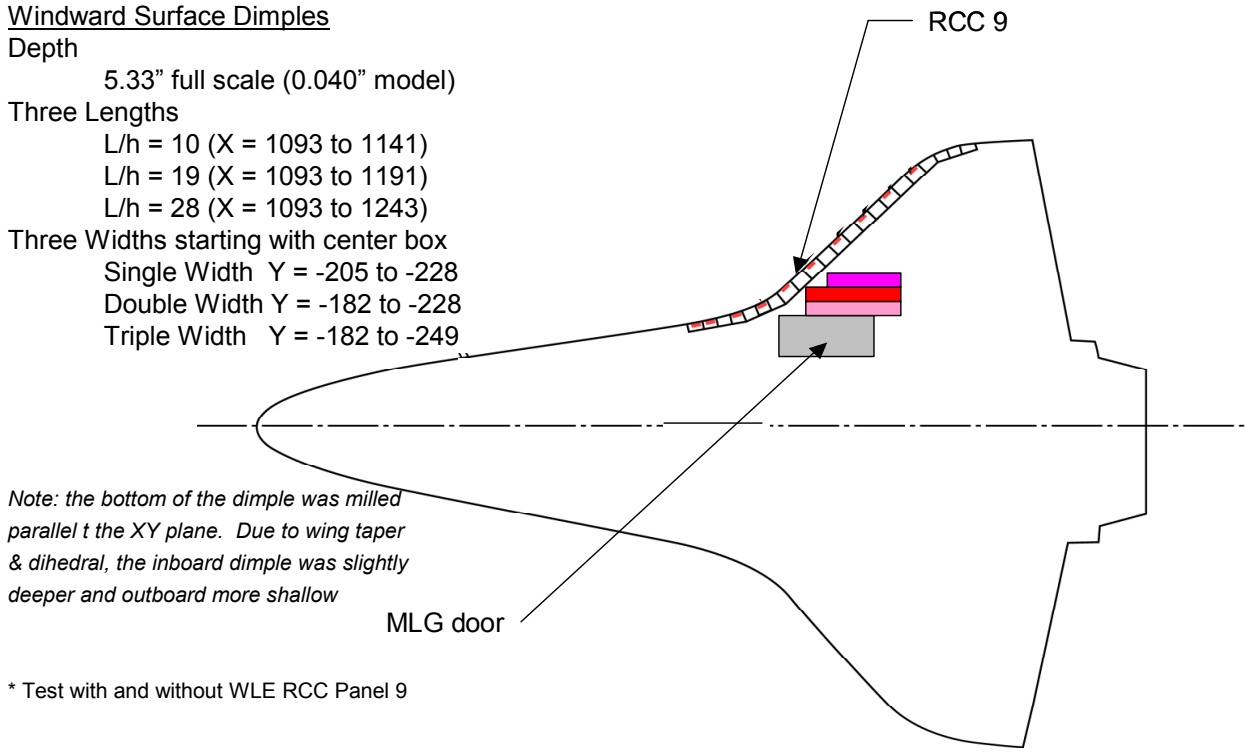

Figure 5-57. LaRC wind tunnel testing of lower surface depressions

Initially, the recessed area would have been relatively small; however, it would gradually grow over time to cause the delta roll moment to increase. By 8:57:29 EST (EI + 800 sec.) wind tunnel testing showed that the depression has to be on the order of 20 feet long, two feet wide, and 5.3 inches deep along with panel 9 missing in order to duplicate the delta roll coefficient shown in Figure 5-50. This configuration provides a delta yaw moment that is slightly larger than was observed, but is consistent with a decreasing negative delta yaw moment observed in this timeframe (Figure 5-51).

A little more than a minute later, at 8:58:44 EST (EI + 875 sec.), the width of this recession would need to have increased by another two feet to match the aerodynamic delta roll and yaw moments. At this point, the rate of change of the aerodynamic moments and damage progression is so great that it likely grew by about an additional two feet in width over the next 25 seconds at 8:59:09 EST (EI + 900 sec.). Additionally, the delta pitch moment was now observed to deviate from previous mission reconstructions in this timeframe. Figure 5-52 shows that the recession concept is

consistent with the delta pitch moment reconstruction. Previous structural analysis indicates that by 8:58:19 EST (EI + 850 sec.) there is large-scale wing deformation and thus the possibility of a large recession is plausible in this timeframe.

In summary, the latest aerodynamic wind tunnel testing and CFD analysis performed to date indicate that the initial damage was probably relatively small, like a hole and/or missing part of the bottom of RCC panel 8. A slot then developed so that there is upward flow through the RCC vent and across the upper 8 carrier panel. Later, more of RCC panel 8 and/or panel 9 is lost along with some substantial wing deformation probably involving a locally depressed area on the lower wing surface. The wing deformation and lower surface recession gradually increased over time, and eventually the yaw and roll moments were too great for the flight control system to manage, leading to a loss of vehicle control and aerodynamic break-up.

Although this aerodynamic reconstruction represents a reasonable sequence of vehicle configurations that led to loss of control during entry, it is not meant to be interpreted as an exact literal sequence of events. The wind tunnel testing and analysis was performed using representative geometries; however, the actual specific vehicle damage is unknown and may never be known completely. The sequence of events discussed here is consistent with the reconstructed aero moments, MADS data, and forensics data and provides the best aerodynamic, thermal, and structural understanding possible for the eventual loss of Columbia.